

# Scattering of exocomets by a planet chain: exozodi levels and the delivery of cometary material to inner planets

Sebastian Marino,<sup>★</sup> Amy Bonsor, Mark C. Wyatt and Quentin Kral

*Institute of Astronomy, University of Cambridge, Madingley Road, Cambridge CB3 0HA, UK*

Accepted 2018 May 24. Received 2018 May 3; in original form 2017 December 20

## ABSTRACT

Exocomets scattered by planets have been invoked to explain observations in multiple contexts, including the frequently found near- and mid-infrared excess around nearby stars arising from exozodiacal dust. Here we investigate how the process of inward scattering of comets originating in an outer belt is affected by the architecture of a planetary system, to determine whether this could lead to observable exozodi levels or deliver volatiles to inner planets. Using  $N$ -body simulations, we model systems with different planet mass and orbital spacing distributions in the 1–50 au region. We find that tightly packed ( $\Delta a_p < 20R_{H,m}$ ) low-mass planets are the most efficient at delivering material to exozodi regions (5–7 per cent of scattered exocomets end up within 0.5 au at some point), although the exozodi levels do not vary by more than a factor of  $\sim 7$  for the architectures studied here. We suggest that emission from scattered dusty material in between the planets could provide a potential test for this delivery mechanism. We show that the surface density of scattered material can vary by two orders of magnitude (being highest for systems of low-mass planets with medium spacing), while the exozodi delivery rate stays roughly constant, and that future instruments such as *JWST* could detect it. In fact for  $\eta$  Corvi, the current Herschel upper limit rules out the scattering scenario by a chain of  $\lesssim 30 M_{\oplus}$  planets. Finally, we show that exocomets could be efficient at delivering cometary material to inner planets (0.1–1 per cent of scattered comets are accreted per inner planet). Overall, the best systems at delivering comets to inner planets are the ones that have low-mass outer planets and medium spacing ( $\sim 20R_{H,m}$ ).

**Key words:** methods: numerical – planets and satellites: dynamical evolution and stability – planets and satellites: general – zodiacal dust – circumstellar matter – planetary systems.

## 1 INTRODUCTION

Planetesimal belts have been inferred in multiple systems to explain the now common infrared (IR) excess found around main-sequence stars, which originates from circumstellar dust (e.g. Su et al. 2006; Hillenbrand et al. 2008; Carpenter et al. 2009; Absil et al. 2013; Eiroa et al. 2013; Matthews et al. 2014; Thureau et al. 2014; Montesinos et al. 2016). Mutual collisions within these Asteroid or Kuiper belt analogues grind down solids sustaining high levels of dust on time-scales as long as Gyr’s, giving rise to debris discs (e.g. Dominik & Decin 2003; Wyatt et al. 2007b).

While most of the systems with cold and warm dust are consistent with Asteroid or Kuiper belt analogues located beyond a few astronomical unit (AU) (e.g. Wyatt et al. 2007b; Schüppler et al. 2016; Geiler & Krivov 2017), a few systems present levels of warm/hot dust detected at near- and mid-infrared (NIR and MIR) wavelengths

(exozodis) that are incompatible with such a scenario (see review by Kral et al. 2017). This is because there are limits on how bright a debris disc can be at any given age (Wyatt et al. 2007a). While at tens of AU, a belt of km-sized or larger planetesimals can survive against collisions on Gyr time-scales, within a few AU debris discs collisionally evolve much faster setting a limit on their brightness. Well-studied systems like the 450 Myr old A-star Vega (Absil et al. 2006; Defrère et al. 2011; Su et al. 2013) and the 1–2 Gyr old F-star  $\eta$  Corvi (Stencel & Backman 1991; Wyatt et al. 2005; Smith, Wyatt & Haniff 2009) have exozodi levels above this limit. This incompatibility implies that the dust in their inner regions or material sustaining it must be either transient, e.g. as a result of a giant collision between planetary embryos or a giant impact on a planet (e.g. Jackson et al. 2014; Kral et al. 2015), or be continually fed from material formed further out in the system where it can survive for much longer time-scales. In fact, this is the case for the zodiacal cloud, much of which is replenished from dust that originates from comets that disintegrate as they pass through the inner Solar system (Nesvorný et al. 2010). Based on the NIR excess

<sup>★</sup> E-mail: [s.marino@ast.cam.ac.uk](mailto:s.marino@ast.cam.ac.uk)

measured in nearby stars using interferometry, it has been estimated that  $\sim 10$ – $30$  per cent of AFGK-type stars have exozodi levels above 1 per cent of the stellar flux (Absil et al. 2013; Ertel et al. 2014), with a tentative correlation with the existence of an outer reservoir of cold dust for FGK-type stars (Nuñez et al. 2017). On the other hand, MIR excesses are less commonly detected (e.g. Kennedy & Wyatt 2013), but at the 1 per cent excess level there again appears to be a correlation with the presence of an outer belt (Mennesson et al. 2014).

Further observational evidence for inward transport of material in planetary systems, but in a different astrophysical context, comes from the presence of elements heavier than He in the atmospheres of  $\sim 30$  per cent of white dwarfs (the so-called polluted white dwarfs, e.g. Zuckerman et al. 2003, 2010; Koester, Gänsicke & Farihi 2014), which suggests that these must be accreting solid material formed beyond a few AU where it could have survived the AGB phase (Farihi et al. 2010; Debes & Sigurdsson 2002). Moreover, some of these polluted white dwarfs also show IR excess and the presence of metallic gas within their Roche limit (e.g. Gänsicke et al. 2006; Melis et al. 2010), indicating the presence of circumstellar material accreting on to the white dwarf.

Different mechanisms have been invoked to explain the bright hot dust, and possibly the white dwarf pollution phenomena: inward scattering of solids from an outer debris belt by a chain of planets (e.g. Bonsor & Wyatt 2012); planetesimals evolving into cometary orbits due to mean motion resonances with an exterior high-mass planet on an eccentric orbit (Beust & Morbidelli 1996; Faramaz et al. 2017); instabilities in the system after which a planet could disrupt a planetesimal belt scattering large amounts of material inwards (similar to the Late Heavy Bombardment in the Solar system; Booth et al. 2009; Bonsor, Raymond & Augereau 2013). The latter has been particularly studied to explain the IR excess around polluted white dwarfs (e.g. Debes & Sigurdsson 2002; Veras et al. 2013).

Alternatively, it has also been considered that exozodis could be fed naturally by the small dust that is continually produced through collisions in an outer debris belt and that migrates in through P-R drag (e.g. van Lieshout et al. 2014; Kennedy & Piette 2015). Moreover, P-R drag models predict that significant amounts of  $\mu\text{m}$ -sized dust should lie within exozodis and outer belts, even in the absence of planets, and distributed with a characteristic flat surface density that could even hinder the characterization of inner planets. However, P-R drag models fail to reproduce the high exozodi levels for some extreme systems such as  $\eta$  Corvi. This is because dust undergoing P-R drag and sublimation does not concentrate in high enough levels in the inner regions, although this could be circumvented by magnetic trapping (Rieke, Gáspár & Ballering 2016).

Understanding the inward transport of material in exoplanetary systems is of great importance as it can set constraints on the architecture of planetary systems (e.g. Bonsor & Wyatt 2012; Bonsor, Augereau & Thébaud 2012), but also it can be used to assess the possibility that material formed at large radii, i.e. rich in volatiles in the form of ices and organic molecules, could be delivered to inner planets via impacts. Impacts and volatile delivery by comets and asteroids originating in the outer asteroid belt have been proposed to account for the water on the Earth as it might have formed dry (Morbidelli et al. 2000; O’Brien, Morbidelli & Levison 2006; Raymond et al. 2009). In the particular case of the Solar system, the formation of Jupiter and Saturn could have been determinant in the delivery of water and volatiles to its inner regions (Raymond & Izidoro 2017). Moreover, impacts could have also acted as chemical activators and the energy source for amino acid formation in primitive atmospheres (e.g. Civi et al. 2004; Trigo-Rodríguez et al.

2017). For other systems with terrestrial planets formed closer in, volatile delivery could be essential for the development of an atmosphere that could support life (e.g. Lissauer 2007; Raymond, Scalo & Meadows 2007). Thanks to the unprecedented sensitivity and resolution of the Atacama Large Millimeter/submillimeter Array (ALMA), it has been possible to detect exocometary gas and constrain the volatile composition of planetesimals in exo-Kuiper belts (e.g. Dent et al. 2014; Kral et al. 2016; Marino et al. 2016; Marino et al. 2017a; Matrà et al. 2017a,b). This supports the general picture that volatiles can be locked in planetesimals (similar to Solar system comets) that could be later delivered to planets (de Niem et al. 2012).

In this paper we study how the scattering of solids (e.g. planetesimals, dust, etc.) varies as a function of the architecture of a planetary system. In particular, we focus on particles on unstable orbits originating from an outer belt (e.g. an exo-Kuiper belt) that get scattered by an outer planet and can continue being scattered to the inner regions of a system by a chain of planets. We use  $N$ -body simulations to investigate:

(i) whether or not exozodis can be produced by the inward scattering of material from an outer planetesimal belt, and how this ability depends on the architecture of the planetary system. There are two observational constraints that must be met, the amount of material delivered to the inner regions must be able to account for the observed excess, and the amount of material in between the outer belt and exozodi must not exceed the upper limits from observations.

(ii) the planetary system architectures that are best suited for delivering material to inner planets, including volatiles locked in ices and organic material.

In Section 2 we describe the general framework of the inward transport problem, and on which aspects we will focus in this paper. In Section 3 we summarize the key factors and considerations that can increase or reduce the inward transport of material via scattering and the number of impacts on inner planets. Then in Section 4 we describe the initial conditions of a set of  $N$ -body simulations that we use to tackle the two points above. Section 5 presents the results from the simulations. In Section 6 we discuss the observability of material being scattered between the planets using current and future instruments and implications for one known system, which systems are potentially the most optimum at producing exozodis and delivering cometary material to inner planets, and we test how a different choice of simulation parameters could affect our results. Finally, Section 7 summarizes our conclusions.

## 2 OUR FRAMEWORK

The process of scattering of particles by a chain of planets that feed an exozodi can be split into three parts (see the sketch in Fig. 1):

(i) Planetesimals are put on unstable orbits near the outermost planet. Planetesimals could be born there or be transported from an outer belt, e.g. via chaotic diffusion (Morbidelli 2005). We simply assume a constant input rate  $R_{\text{in}}$ .

(ii) Planetesimals are scattered by the chain of planets resulting in ejections, accretion on to planets, or inward transport.

(iii) The solid mass in planetesimals that gets to the inner regions where the exozodi lies is assumed to be transformed into dust and removed. This could happen through sublimation of ices or disruption events, releasing dust as Solar system comets, or through mutual collisions in a so-called collisional cascade.

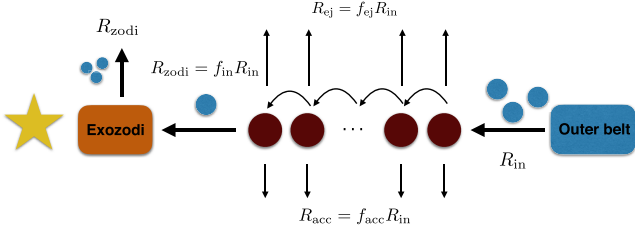


**Figure 1.** Sketch of a planetary system (planets as brown circles) scattering planetesimals (blue circles) that are input near the outermost planet at a rate  $R_{in}$ , get ejected at a rate  $R_{ej}$ , accreted by planets at a rate  $R_{acc}$ , and get to the inner regions at a rate  $R_{zodi}$ . Once in the inner regions, we assume that planetesimals are processed into small dust that is lost, e.g. via radiation pressure or P-R drag.

In this paper we focus on studying the second stage (ii). We want to test the analytic predictions from previous work (see Section 3 below) and investigate further the process of scattering by multiple planets on circular orbits. We assume that particles are already on unstable orbits, or equivalently, they are input near the outermost planet at a constant rate  $R_{in}$  (see possible scenarios in Section 6.5). We follow the different outcomes of particles being scattered and we trace the number of particles that get ejected, accreted, and that reach the exozodi region. We assume that particles are lost immediately after reaching this exozodi region (or rather on a time-scale much shorter than their orbital evolution). This is the most optimistic scenario as in reality only a fraction of the mass would end up as exozodiacal dust.

### 3 SCATTERING CONSIDERATIONS

In this section, we describe the results from previous studies that we use to make predictions regarding how the scattering process depends on the architecture of a planetary system. The basic condition for a particle to be scattered by a planet is that their orbits must cross or get sufficiently close in order to have a close encounter. For a planet on a circular orbit, this translates to a condition on the planet’s semimajor axis ( $a_p$ ) and on the semimajor axis and eccentricity of the particle ( $a$  and  $e$ , respectively), i.e.

$$a(1 + e) \gtrsim a_p - 1.5R_H = Q_{min} \text{ if } a < a_p, \quad (1)$$

or

$$a(1 - e) \lesssim a_p + 1.5R_H = q_{max} \text{ if } a > a_p, \quad (2)$$

where  $R_H = a_p(M_p/(3M_\star))^{1/3}$  is the planet’s Hill radius and  $M_p$  is the planet mass. The factor preceding  $R_H$  should be of the order of unity and is arbitrarily set to 1.5 to match the results presented below. Particles that satisfy this condition can be scattered by the planet diffusing in energy or  $1/a$  (e.g. Duncan, Quinn & Tremaine 1987). Below we present the main analytic considerations and predictions from previous works that we will test with our simulations.

#### 3.1 Planet spacing – multiple scattering

Particles scattered by only one planet on a circular orbit will be constrained by the Jacobi constant or Tisserand parameter ( $T_p$ ; Tisserand 1896; Murray & Dermott 1999), which is conserved in the circular restricted three-body problem when  $M_p \ll M_\star$ . The Tisserand parameter can be written as

$$T_p = \frac{a_p}{a} + 2\sqrt{\frac{(1 - e^2)a}{a_p}} \cos(I), \quad (3)$$

where  $I$  is the particle’s inclination. Particles with  $T_p \lesssim 3$  can get sufficiently close to a planet (e.g. within a Hill radius) to experience a close encounter. As shown by Bonsor & Wyatt (2012), the condition for scattering together with the conservation of  $T_p$  implies that a particle being scattered by a single planet on a circular orbit will be constrained in the  $a - e$  space. Specifically, given the restriction in equation (1), zero inclination and assuming  $2 < T_p < 3$ , there is a minimum pericentre that a particle can reach ( $q_{min}$ ) given by

$$q_{min} = \frac{-a_p Q_{min} T_p^2 + 2a_p^2 T_p + 4Q_{min}^2 - 4\sqrt{2a_p^3 Q_{min} - a_p^2 Q_{min}^2 T_p + Q_{min}^4}}{a_p T_p^2 - 8Q_{min}}. \quad (4)$$

Equation (4) implies that particles initially in low-eccentricity orbits ( $e_p \lesssim 0.3$ ) cannot reach the very inner regions if their Tisserand parameter is conserved, i.e. when being scattered by a single planet.

There are multiple ways around this restriction. Particles could arrive near the scattering region of the planet with high eccentricities or inclinations, i.e. low  $T_p$ , for example if originating in an exo-Oort cloud. Alternatively, the presence of additional planets could modify the initial Tisserand parameter of particles if these get scattered by multiple planets, in which case there is a constraint on the separation of the additional planets (Bonsor & Wyatt 2012). This is the scenario that is considered in our modelling approach.

Assuming particles start with low eccentricity and inclinations near the outermost planet (which is the case for our simulations), for efficient inward scattering the next planet in the chain must have a semimajor axis larger or near  $q_{min, p1}$ , which is the minimum pericentre that particles can reach when scattered by the outermost planet (‘p1’). If not, inward scattering may still occur since particles could have their Tisserand parameter modified via secular perturbations or resonances from the additional planets, although these act on longer time-scales. Therefore, assuming particles start on orbits with low  $e$  and  $I$ , and near planet p1 ( $T_{p1}$  close to 3), our first consideration for a chain of planets to optimally scatter particles inwards from an outer belt is that their two outermost planets must be in orbits near to each other. The closer they are, the higher the number of particles with  $T_{p1}$  small enough to reach the next planet in the chain. If particles are initially in highly eccentric or inclined orbits, e.g. Oort cloud objects, their Tisserand parameter will be low enough such that the separation between the planets is no longer a constraint.

To illustrate the scattering restriction, Fig. 2 shows curves of constant Tisserand parameter (solid lines) as a function of semimajor axis and eccentricity with respect to two  $30 M_\oplus$  planets on circular orbits with  $a_p = 20, 50$  au (orange and blue, respectively). Assuming particles in the system are initially in the vicinity of the outermost planet (denoted as p1), their final outcome will depend on their initial Tisserand parameter with respect to p1. For example,  $T_{p1} \gtrsim 3.0$  particles will form a scattered disc constrained within  $a_p = 35\text{--}80$  au and since particles with eccentricities lower than 0.4 will never have a close encounter with the second planet (p2), these will not make it to the inner regions. Otherwise,  $T_{p1} \lesssim 2.97$  particles can reach a pericentre near 20 au and be scattered by p2 (which then changes their  $T_{p1}$ ). Multiple scattering can put particles on highly eccentric orbits that can reach the inner regions (in grey for those reaching a radius smaller than 1 au), or get eventually ejected from the system. This condition is met in the Solar system, where Uranus is close enough to Neptune such that particles in the Kuiper belt with  $T_{Nep} < 2.999$  can be scattered by Uranus after a few encounters with

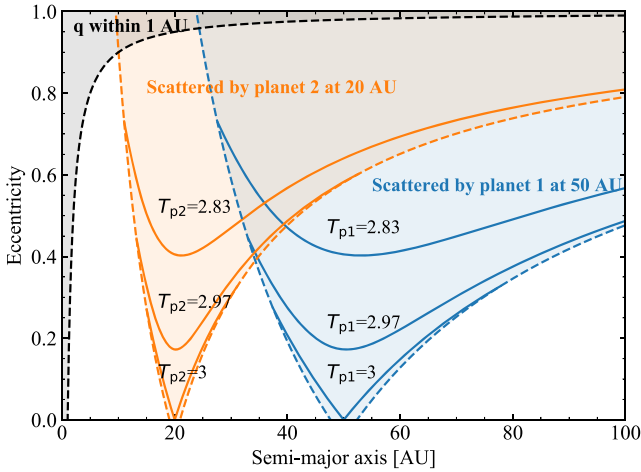


**Figure 2.** Constant Tisserand parameter curves and scattering regions for two  $30 M_{\oplus}$  planets in circular orbits and with semimajor axes of 50 (i, blue) and 20 au (ii, orange). The dashed lines correspond to the scattering regions, i.e. orbits crossing  $a_p \pm 1.5R_H$ . The continuous lines represent curves of constant Tisserand parameter with respect to planets i and ii, and assuming  $I = 0$ . The black dashed line shows the semimajor axes and eccentricities of particles that have a pericentre lower than 1 au.

Neptune (e.g. Levison & Duncan 1997). Additional planets could be present closer in which could help to increase the inward flux of scattered particles.

### 3.2 Planet masses – time-scales

The second consideration relates the mass distribution of planets as a function of semimajor axis. As stated by Wyatt et al. (2017), particles will be passed inwards more efficiently when interior planets start dominating the scattering process, i.e. when the scattering time-scale is shorter for interior planets. The scattering time-scale can be approximated by the cometary diffusion time (Brasser, Duncan & Levison 2008)

$$t_{\text{scat}} \cong M_{\star}^{3/2} a_p^{3/2} M_p^{-2}, \quad (5)$$

where  $M_p$  is in units of the Earth masses,  $a_p$  in au,  $t_{\text{scat}}$  in Gyr, and  $M_{\star}$  is the mass of the central star in solar masses. Since these time-scales increase with orbital radius and decrease with planet mass, chains of planets with equal mass or decreasing as a function of radius should be more efficient at passing particles inwards.

If particles are born near the outermost planet in the chain, that planet’s mass will determine the time-scale and rate at which particles are scattered in. For example, if the scattering time-scale is longer or of the order of the age of a system, then planet scattering can sustain an exozodi at the current age of the system relying solely on planetesimals formed in its vicinity. Otherwise, the exozodi fed by scattered primordial particles would only last a fraction of the age of a system. Using  $N$ -body simulations, Bonsor et al. (2012) studied this considering chains of equal mass planets and how their masses can affect the process of inward scattering when particles start in the unstable region near the outermost planet. They found that while higher mass planets can scatter material inwards at a higher rate, lower mass planets continue to scatter material inwards on longer time-scales as they clear their orbits on a longer time-scale. Therefore, in order to sustain high exozodiacal dust levels for 0.1–1 Gyr from planetesimals born near the outermost planet, a

massive outer belt and a chain of tightly packed low-mass planets were necessary.

Similarly, using analytical arguments Wyatt et al. (2017) considered that in order to maximize the inward flux in a system at a given age, no planets should lie in the *ejected* region in the  $a_p - M_p$  space. In this region planets can eject particles on a time-scale (approximated by the cometary diffusion time-scales) shorter than the age of the system, and thus might never get to the inner regions before being ejected, or if they do, they will be quickly removed. However, the effect of a complex multiplanet system on this simple argument has to be investigated.

An important caveat is that implicit in the arguments above is that planetesimals were born near the outermost planet. The scenario that we are considering in this paper is that particles are continually input near the outermost planet. This means that both of the above constraints are relaxed (i.e. the scattering time-scale for the outermost planet, and those closer in, can potentially be shorter than the system age and still result in material reaching the inner regions at a given age). However, for planets that are very low in mass, the orbits of particles will still evolve on time-scales much longer than the age of the system, thus, being unable to scatter particles in at a high rate and setting a lower limit on the mass of the outermost planet. For example, particles scattered by a  $5 M_{\oplus}$  planet at 50 au will evolve on time-scales of  $\sim 10$  Gyr.

To conclude, we expect that the best systems for scattering particles inwards from an outer belt should be the ones with equal mass planets or decreasing mass with orbital radius. If we additionally require that the particles being scattered are born in the vicinity of the outermost planet (which is not the case here), then that outermost planet should also lie below the ejected region for the age of the system.

### 3.3 Planet masses and relative velocities – accretion

The third consideration relates to the possibility of particles being accreted by planets, possibly delivering volatiles to the inner planets. To quantify the number of particles that will be accreted by a planet, or the rate at which they will, it is necessary to consider the mass and radius of the planet (which define its collisional cross-section), the volume density of particles that the planet encounters, and the encounter velocities. If the system is continually fed from particles starting in the outer regions (the scenario that we are considering here), these will then form what we will call a *scattered disc*, with a density of particles that will reach a steady state. This density represents the amount of material that can potentially be accreted at any given time and orbital radius. It will depend both on the amount of material that is passed in from the outermost planet to the inner regions, and on its lifetime before being lost, e.g. via ejection or on to the rest of the planets in the system. The rate at which a planet accretes can be approximated as

$$R_{\text{acc,p}} = \frac{v_{\text{rel}} \Gamma \Sigma(r)}{h}, \quad (6)$$

where  $\Gamma$ ,  $\Sigma(r)$ ,  $v_{\text{rel}}$ , and  $h$  are the collisional cross-section of the planet, the steady-state surface density of particles (number per unit area), the relative velocity between a planet and particles, and the scale height of the scattered disc, respectively. The latter can be approximated by the product of  $r$  and the average inclination  $\langle I \rangle$  of the particles orbits. Both  $\Sigma(r)$  and  $h$  are determined by the specific architecture of the planetary system. For example, particles being scattered by low-mass planets are likely to survive for longer time-scales against ejection, increasing  $\Sigma(r)$ . The collisional cross-

section is defined by the mass and radius of the planet, together with the relative velocities, as

$$\Gamma = \pi R_p^2 \left( 1 + \frac{v_{\text{esc}}^2}{v_{\text{rel}}^2} \right), \quad (7)$$

where  $R_p$ ,  $v_{\text{esc}}$ , and  $v_{\text{rel}}$  are the radius of the planet, its escape velocity, and relative velocity before the encounter, respectively. The higher  $\Gamma$  is, the higher the rate of impacts on that planet (equation 6). For  $v_{\text{esc}} \gg v_{\text{rel}}$  and  $M_p \propto R_p^3$  (i.e. fixed density), we find  $\Gamma \propto M_p^{4/3}$ , otherwise  $\Gamma \propto M_p^{2/3}$ . Therefore,  $R_{\text{acc}, p}$  will be greater for more massive planets as these have greater radii and escape velocities (i.e. greater  $\Gamma$ ), lower relative velocities (greater  $\Gamma$  and lower  $h$ ), and higher surface densities.

However, it is unclear how the mass distribution of planets will also affect the density of particles (determined by the inward scattering and particles lifetimes) and their relative velocities, with the latter mainly defined by the distribution of eccentricities and inclinations. We can guess that chains of more massive planets will result in lower  $\Sigma(r)$  and higher relative velocities because particles are easily put on highly eccentric/inclined orbits. As shown by Wyatt et al. (2017), the most likely outcome of particles being scattered by a planet can be understood by comparing the planet's Keplerian velocity ( $v_k$ ) with its escape velocity  $v_{\text{esc}}$ . This is because the maximum kick that a particle can experience after a single scattering event is of the order of  $v_{\text{esc}}$ , since to get a larger kick it would have to come so close that it would hit the planet. Therefore, if  $v_{\text{esc}} \gg v_k$ , particles are likely to be ejected in a few close encounters, decreasing the surface density of the scattered disc. Otherwise particles would need a large number of encounters before being ejected, increasing the surface density of the scattered disc and the likelihood of being accreted by a planet. Equating  $v_{\text{esc}}$  and  $v_k$ , we find (equation 1 in Wyatt et al. 2017)

$$M_p \cong 40 M_\star^{3/2} a_p^{-3/2} \rho_p^{-1/2}, \quad (8)$$

where  $\rho_p$  is the bulk density of the planet in units of  $\text{g cm}^{-3}$  and  $M_p$  is in units of  $M_\oplus$ . Planets below this mass are likely to accrete particles if these are not lost on shorter time-scales via other means.

### 3.4 Predictions

To summarize, assuming particles are input at a constant rate in the vicinity of the outermost planet, we predict the following based on previous studies:

(i) Systems with outer planets close to each other will be better at scattering particles inwards as more particles will have a low enough Tisserand parameter to reach the second outermost planet (equation 4).

(ii) Higher mass planets will scatter and eject particles on shorter time-scales (equation 5) and could result in inefficient inward scattering.

(iii) In order to scatter particles inwards, scattering time-scales of the inner planets must be shorter than those further out, as shown by equation (5). These can be achieved by planet chains of equal mass or decreasing mass with orbital radius.

(iv) Planets will accrete more particles if they are more massive, if the surface density of particles around their orbits is higher, and if particles are on low-eccentricity and low-inclination orbits, i.e. low relative velocities (equations 6 and 7).

There is no analytic prediction for how the surface density will change when varying the planet masses as it depends both on the

scattering time-scale and on the inward flux of material. Moreover, the inward flux, distribution of eccentricities and inclinations, and accretion on to planets could vary as a function of the spacing between the planets.  $N$ -body simulations are well suited to study these effects and test the predictions above.

## 4 N-BODY SIMULATIONS

In order to test our predictions presented above, and quantify how the mass distribution and orbit spacing of a chain of planets affect the inward transport of particles being scattered, we simulate such interactions using  $N$ -body simulations. We model the gravitational interactions with the  $N$ -body integrator MERCURY 6.2 (Chambers 1999), using the hybrid symplectic/Bulirsch–Stoer integration algorithm. This allows us to speed up the simulations computing distant interactions quickly, without losing precision in close encounters. Our systems are composed of a  $1 M_\odot$  star, a chain of planets, and  $10^3$  massless particles. The simulations lasted 1 Gyr, long enough such that the majority of the particles are lost via ejections and accretion on to the star or planets. Outputs or snapshots of the simulations are saved every  $10^4$  or  $10^5$  yr, which we estimate is shorter than the scattering diffusion time-scale for most of our simulations (see Section 4.1 below). We set an outer boundary of  $10^3$  au and an inner boundary of 0.5 au, i.e. particles are removed from the simulation when their apocentre is larger than  $10^3$  au or their pericentre is lower than 0.5 au. The latter is set to trace the number of particles that are able to reach the innermost regions that we are interested in, and also because our time-step of 30 d is not small enough to accurately integrate the orbits within this boundary. This assumes that particles are lost as soon as they reach within this boundary by being incorporated into the exozodi. Each simulation is run 20 independent times with random mean anomalies, longitudes of ascending node and pericentres, and splitting the total number of massless particles (50 test particles for each).

### 4.1 Planet mass and semimajor axis distribution

We consider a chain of planets on circular co-planar orbits, with masses varying from 1 to  $200 M_\oplus$  ( $0.63 M_{\text{Jup}}$ ) and semimajor axes between 1 and 50 au. We assume densities of  $1.6 \text{ g cm}^{-3}$  (Neptune's density). As we are interested in studying how the scattering process depends on the mass distribution and spacing of planets, we parametrized their masses as a function of  $a_p$ , and their spacings or separations as a function of  $a_p$  and their mutual Hill radius ( $R_{H, m}$ ). More specifically, we defined

$$M_p(a_p) = M_0 \left( \frac{a_p}{a_0} \right)^{\alpha_M}, \quad (9)$$

where  $M_0$ ,  $a_0$ , and  $\alpha_M$  define the planet masses in the chain. The semimajor axis of the planets is defined such that  $a_p = 50$  au for the outermost planet and the separation between their orbits is

$$\Delta a = K(a_{p1}, a_{p2}) R_{H, m}, \quad (10)$$

$$K(a_{p1}, a_{p2}) = K_0 \left( \frac{a_{p1} + a_{p2}}{2a_0} \right)^{\alpha_\Delta}, \quad (11)$$

where  $K_0$  and  $\alpha_\Delta$  control the separation of the planets and their long-term stability. We add planets in the system from 50 to 1 au using equations (9) and (11). The initial mean anomaly of every planet is chosen randomly such that each simulated system is run on 20 slightly different configurations.

Our reference chain of planets has  $M_0 = 30 M_{\oplus}$ ,  $a_0 = 10$  au,  $\alpha_M = 0$ ,  $\alpha_{\Delta} = 0$ , and  $K_0 = 20$ . This defines a reference to which we compare when varying the different parameters. We vary  $M_0$  between 10 and 90  $M_{\oplus}$  to study chains of low- and high-mass planets,  $\alpha_M$  between  $-1$  and  $1$  to study the effect of decreasing or increasing planet mass as a function of  $a_p$ ,  $\alpha_{\Delta} = 0.3$  and  $-0.3$  (such that no pair of planets is closer than  $10 R_{H,m}$ ) to study the effect of planet spacing varying with  $a_p$ , and  $K_0$  between 8 and 30 to study the differences between tightly packed systems and widely spaced systems. The range of spacings is inspired by the spacing distribution found for *Kepler* close in multiplanet systems, where spacings between 10 and 30 mutual Hill radii are the most common (Fang & Margot 2013; Pu & Wu 2015; Weiss et al. 2018), although this is uncertain for planets at large orbital radii. In addition, if  $K < 10$  the system could go unstable on a time-scale shorter than 1 Gyr (Chambers, Wetherill & Boss 1996; Smith & Lissauer 2009). Table 1 and Fig. 3 summarize the 10 main planet configurations that we explore. In the same figure, the dashed black lines represent the mass above which planets are more likely to eject particles rather than accrete (equation 8), while the continuous black lines represent the scattering diffusion time-scale or the planet masses above which particles are ejected on a time-scale shorter than 1 Gyr, 10 Myr, and 100 kyr (equation 5). In all the configurations, there are planets that will eject particles on time-scales shorter than or of the order of 1 Gyr, the length of our simulations.

## 4.2 Massless particles distribution

Particles are initially distributed in a cold disc, with eccentricities and inclinations uniformly distributed between  $0$ – $0.02$  and  $0$ – $10^\circ$ , respectively.<sup>1</sup> As we are interested only in those particles that can be scattered, we initialized all of them in the outermost planet’s chaotic zone, i.e. the unstable region of semimajor axes surrounding the planet in which mean motion resonances overlap. The size of the chaotic zone has been analytically estimated to be (Wisdom 1980)

$$\delta_{\text{chaos}} = 1.3 a_p \left( \frac{M_p}{M_*} \right)^{2/7}. \quad (12)$$

Within this zone, eccentricities are excited and initially non-crossing orbits start to cross the planet’s orbit, or get sufficiently close to have close encounters and be scattered by the planet. We initialized all the particles with semimajor axes ( $a_p$ ) uniformly distributed within  $a_{\text{pl}}^i \pm \delta_{\text{chaos}}$  ( $\sim 45$ – $55$  au for a  $30 M_{\oplus}$  planet at 50 au). This ensures that particles will be dynamically excited and likely to be scattered early on during the simulation.

The initial distribution of orbital parameters sets the range of Tisserand parameters that the particles have with respect to the outermost planet (p1). For a  $30 M_{\oplus}$  planet,  $T_{p1}$  is initially distributed between 2.97 and 3.01 (in Section 6.6 we discuss the effect of varying the initial  $e$  and  $i$ ). The minimum  $T_{p1}$  is the same for all our simulations as it is set approximately by the particles with semimajor axis equal to that of the planet (if  $e$  and  $i$  are small). On the other hand, the maximum  $T_{p1}$  is set by particles at the inner and outer edges of the chaotic zone whose size increases with planet mass, therefore the maximum  $T_{p1}$  is higher for more massive planets and scales approximately as  $3 + 5(M_p/M_*)^{4/7}/4$ . As explained in Section 3, the minimum Tisserand parameter sets the minimum pericentre ( $q_{\text{min}, p1}$ ) that scattered particles can have after multiple scattering events by the outermost planet, and thus, if they can be

readily scattered by the second outermost planet. The latter enables the further inward scattering that we are interested in.

In Fig. 3 we show  $q_{\text{min}, p1}$  (vertical dashed lines) as a reference to identify those configurations that we expect not to be optimal for inward scattering, i.e. those systems in which the second outermost planet has semimajor axis lower than the minimum pericentre of particles when interacting only with the outermost planet. This pericentre is calculated using equation (4) and setting  $a_p = a_{p1}$ ,  $Q_{\text{min}} = a_{p1} - 1.5R_H$ , and  $T_p = \min(T_{p1})$ , where the minimum Tisserand parameter is approximately 2.97. For low planet masses and  $T_{p1} = 2.97$ , we find  $q_{\text{min}, p1} \approx a_{p1}/2 - 9R_H/2$ , thus lower for higher planet masses. We anticipate that planet configurations 4 and 8 from Table 1 (red and light green in Fig. 3) will be very inefficient at inward scattering because their outermost planets are too separated under this criterion.

While our simulations assume that particles start near the outermost planet on low eccentricity and inclination orbits, the exact distribution of eccentricities and inclinations would depend on the specific mechanism that is inputting particles near the outermost planet. Hence, a caveat in what follows is that we are assuming that the particles’ initial conditions described above are a good approximation to their orbits at the start of the scattering process. The specific mechanism inputting particles and initial conditions are discussed in Sections 6.5 and 6.6.

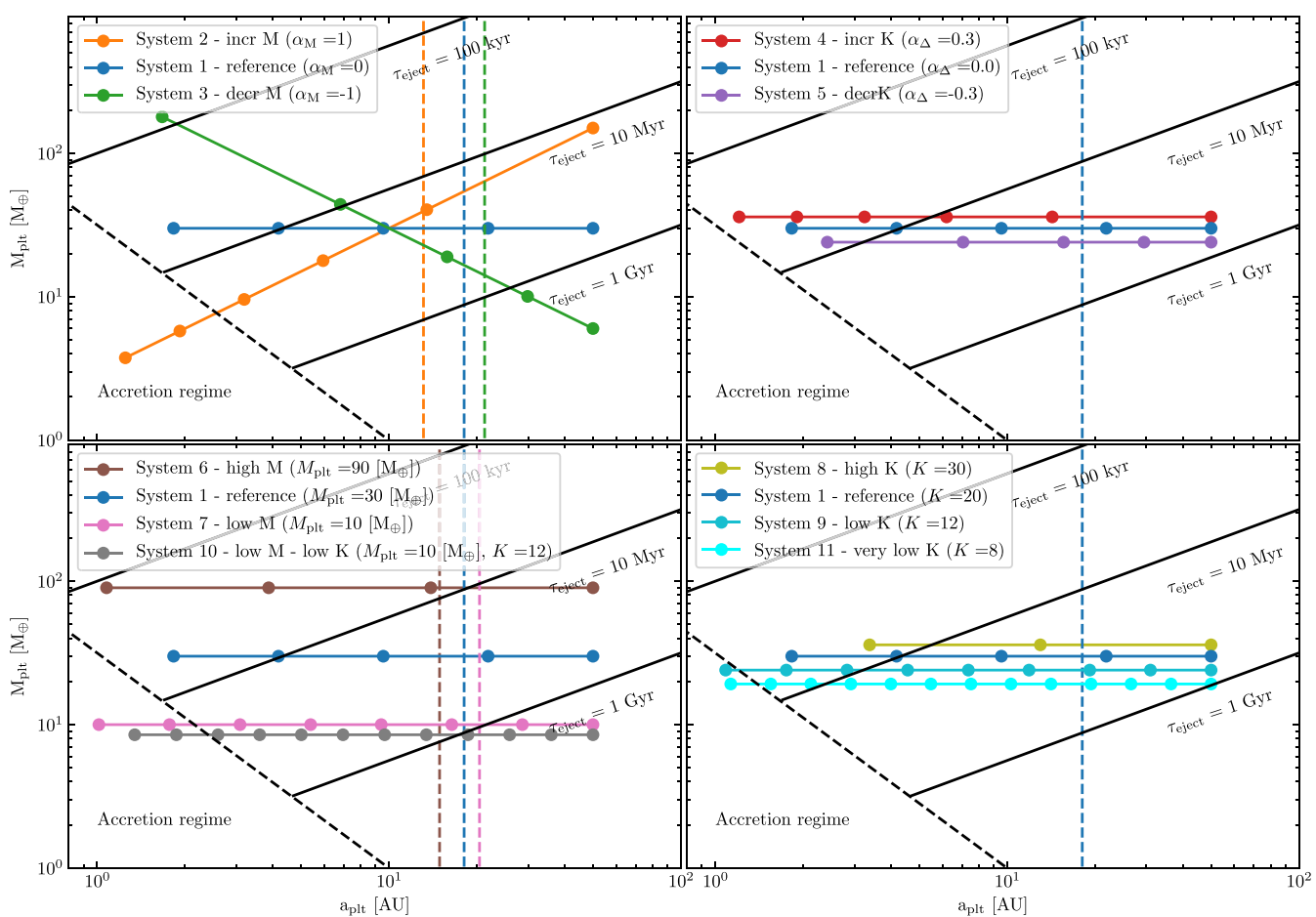
## 4.3 Analysis of simulations

For each simulation, we first remove those particles that were initially in stable tadpole and horseshoe orbits (hereafter called Trojans,  $N_{\text{Troj}}$ ). We identify Trojan particles as the ones that after 1 Myr of evolution lie within 1.2 Hill radii from the outermost planet and with an eccentricity lower than 0.03 (typically 20–30 per cent of simulated particles). Then we follow the evolution of the rest of the particles (a total number  $N_{\text{tot}}$ ) and trace the number of particles ejected ( $N_{\text{ej}}$ ), that cross the inner boundary at 0.5 au ( $N_{\text{in}}$ ), and that were accreted by planets ( $N_{\text{acc}}$ ). We compare these between the different simulations by dividing by the total number of particles that are lost during 1 Gyr of evolution ( $N_{\text{lost}} = N_{\text{ej}} + N_{\text{in}} + N_{\text{acc}}$ ). We divide by  $N_{\text{lost}}$  rather than by  $N_{\text{tot}}$  (the total number of simulated particles) because the time-scales at which particles evolve in some of the simulated systems are comparable to 1 Gyr, hence a significant number of particles have not been lost by the end of the simulation. These particles (a total of  $N_{\text{tot}} - N_{\text{lost}}$ ) remain in the system in highly eccentric and inclined orbits (i.e. in the scattered disc). Hence, we compare the fraction of particles ejected ( $f_{\text{ej}} = N_{\text{ej}}/N_{\text{lost}}$ ), that cross the inner boundary ( $f_{\text{in}} = N_{\text{in}}/N_{\text{lost}}$ ) and that are accreted by planets ( $f_{\text{acc}} = N_{\text{acc}}/N_{\text{lost}}$ ). We also compute the fraction of particles accreted per inner planet ( $f_{\text{acc}, p}$ ), defined as those with  $a_p < 10$  au. Comparing these relative fractions is equivalent to extrapolating to  $t = \infty$  assuming that the remaining particles will be lost via ejection, accretion, or crossing the inner edge in the same proportions as the particles that are lost by 1 Gyr, i.e. this is equivalent to assuming that  $f_{\text{ej}}, f_{\text{in}}, f_{\text{acc}}$  stay constant over time. This is not necessarily the case as most of the particles remaining are typically in an outer scattered disc with large semimajor axes, where they could be more likely to be ejected than when they started near the outermost planet. However, this helps to give an idea of the absolute fractions if simulations were run for longer and is shown to be representative in one of the simulations (the one with lowest mass planets) that was run for 5 Gyr in Section 6.6. We also report uncertainties on  $f_{\text{ej}}, f_{\text{in}}, f_{\text{acc}}$ , etc. based on 68 per cent Poisson confidence

<sup>1</sup>Note that this choice is arbitrary and its effect is discussed in Appendix A.

**Table 1.** Set-ups of the different  $N$ -body simulations varying  $M_0$  (planet mass at 10 au),  $\alpha_M$  (planet mass semimajor axis dependence),  $K_0$  (planet spacing at 10 au in mutual Hill radii), and  $\alpha_\Delta$  (planet spacing semimajor axis dependence).  $N_p$  is the number of planets in each simulated system.

| Number | Label         | Colour     | $\alpha_M$ | $\alpha_\Delta$ | Masses ( $M_\oplus$ )   | $a_p$ (au)  | $\Delta a/R_{H,m}$   | $N_p$ |
|--------|---------------|------------|------------|-----------------|-------------------------|---|----------------------|-------|
| 0      | single planet | black      |            |                 | 30                      | 50.0  | –                    | 1     |
| 1      | reference     | dark blue  | 0.0        | 0.0             | 30                      | (1.8, 4.2, 9.6, 21.9, 50.0)   | 20                   | 5     |
| 2      | incr M        | orange     | 1.0        | 0.0             | (4, 6, 10, 18, 40, 150) | (1.2, 1.9, 3.2, 5.9, 13.5, 50.0)  | 20                   | 6     |
| 3      | decr M        | green      | -1.0       | 0.0             | (180, 44, 19, 10, 6)    | (1.7, 6.8, 15.8, 29.9, 50.0)  | 20                   | 5     |
| 4      | incr K        | red        | 0.0        | 0.3             | 30                      | (1.2, 1.9, 3.2, 6.2, 14.3, 50.0)  | (11, 13, 16, 20, 28) | 6     |
| 5      | decr K        | purple     | 0.0        | -0.3            | 30                      | (2.4, 7.1, 15.6, 29.4, 50.0)  | (25, 19, 16, 13)     | 5     |
| 6      | high M        | brown      | 0.0        | 0.0             | 90                      | (1.1, 3.9, 13.9, 50.0)  | 20                   | 4     |
| 7      | low M         | pink       | 0.0        | 0.0             | 10                      | (1.0, 1.8, 3.1, 5.4, 9.4, 16.4, 28.7, 50.0)                             | 20                   | 8     |
| 8      | high K        | yellow     | 0.0        | 0.0             | 30                      | (3.4, 13.0, 50.0)   | 30                   | 3     |
| 9      | low K         | light blue | 0.0        | 0.0             | 30                      | (1.1, 1.8, 2.8, 4.6, 7.4, 11.9, 19.2, 31.0, 50.0)                       | 12                   | 9     |
| 10     | low M – low K | grey       | 0.0        | 0.0             | 10                      | (1.3, 1.9, 2.6, 3.6, 5.0, 7.0, 9.7, 13.4, 18.7, 25.9, 36.0, 50.0)       | 12                   | 12    |
| 11     | very low K    | light blue | 0.0        | 0.0             | 30                      | (1.1, 1.6, 2.1, 2.9, 4.0, 5.5, 7.5, 10.3, 14.1, 19.4, 26.6, 36.5, 50.0) | 8                    | 13    |


**Figure 3.** Masses and semimajor axes of planets in each simulated system. *Upper left panel:* chains of planets with varying  $\alpha_M$ . *Upper right panel:* chains of planets with varying  $\alpha_\Delta$  (the mass of the planets is offset for display). *Lower left panel:* chains of equal mass planets of 10, 30, and 90  $M_\oplus$  and separations of 20 or 12 mutual Hill radii. *Lower right panel:* chains of equal mass planets with  $K_0 = 12, 20,$  and  $30$ . The dots represent the position of the planets. The vertical dashed lines represent the minimum pericentre of particles scattered by the outermost planet given their initial Tisserand parameter (equation 4). The dashed black lines represent the mass above which planets are more likely to eject particles rather than accrete (equation 8). The continuous lines represent the planet mass above which particles are ejected on a time-scale shorter than 1 Gyr, 10 Myr, and 100 kyr (equation 5). Planet masses of systems 4, 5, 8, 9, and 10 have been scaled by 20 and 36 per cent for a better display.

intervals (16th and 84th percentiles) using analytic approximations from Gehrels (1986).

In order to quantify how fast particles are lost, we also compute the half-life of ejected particles,  $t_{ej}$ . This is defined as the time it takes to eject half of the total number of particles expected to be ejected by  $t = \infty$ , assuming  $N_{ej}$  will tend to  $f_{ej}N_{tot}$  by the end of the simulation (i.e. assuming that  $f_{ej}$  is constant over time).

We are also interested in the spatial distribution or surface density distribution of scattered particles within the chain of planets, i.e. from 1 to 50 au. Because the distribution of particles evolves with time (see Sections 5.1 and 5.2) and on different time-scales for each planet configuration, we focus on the steady-state surface density of scattered particles,  $\Sigma(r)$ . This assumes that particles are input in the system at a constant rate inside the chaotic zone of the outermost planet. In order to use the simulation results to mimic a steady-state input scenario, we take each particle and randomize its initial epoch (originally  $t = 0$ ) to a value between 0 and 1 Gyr. Once a Gyr is reached (the initial integration time), we loop the particle's later evolution to  $t = 0$ . In order to minimize random effects caused by the finite number of particles used in these simulations ( $\sim 700$  excluding Trojans) used in these simulations, we effectively mimic each particle 200 times by randomizing in terms of mean anomaly at each time-step. This leads to an effective  $\sim 140\,000$  particles used to calculate the surface density distribution at each epoch. We then average the surface density over time to obtain the average steady-state surface density distribution  $\Sigma(r)$ . We estimate the uncertainty on  $\Sigma(r)$  by computing the variance of  $\Sigma(r, t)$  averaged over 100 Myr time bins (i.e. from 10 data points at each orbital radius). Finally, because  $\Sigma(r)$  is proportional to the mass input rate (the same for all our simulations), in our analysis we compare  $\Sigma(r)$  divided by the mass input rate. Then the surface density can be obtained by multiplying by any mass input rate. Below, we will also use the surface density at 10 au,  $\Sigma(10\text{ au})$ , as a metric to compare different systems.

## 5 RESULTS

In this section, we present the main results from each simulation. We first describe the results of a case with a single  $30 M_{\oplus}$  planet at 50 au (Section 5.1) and our reference chain of equal mass planets (Section 5.2). Then, we present results for planet configurations of equal planet mass, but varying their spacing (Section 5.3), and configurations with constant spacing in mutual Hill radii, but varying their masses (Section 5.4). In Section 5.5, we discuss our results in the context of the predictions made in Section 3.

### 5.1 Single-planet system

In the single-planet system, we find that of the total number of particles lost, 85 per cent of particles are ejected, 15 per cent are accreted by the planet, and none cross the 0.5 au inner edge. The ejection time-scale is 380 Myr, consistent with the 390 Myr scattering time-scale estimated with equation (5). After 1 Gyr of evolution, 17 per cent of particles remain in the system on highly eccentric orbits, most of which have semimajor axes beyond 50 au. As noted in Section 4.3, these fractions exclude Trojans which represent 31 per cent of the original  $10^3$  simulated particles. The top panel in Fig. 4 shows the evolution of the surface density of particles when they all start near the outermost planet at  $t = 0$  (colours) and the steady-state surface density when particles are input at a constant rate (black). In all cases the surface density peaks near 50 au (where particles are initially placed). Beyond 50 au,  $\Sigma(r)$  decreases

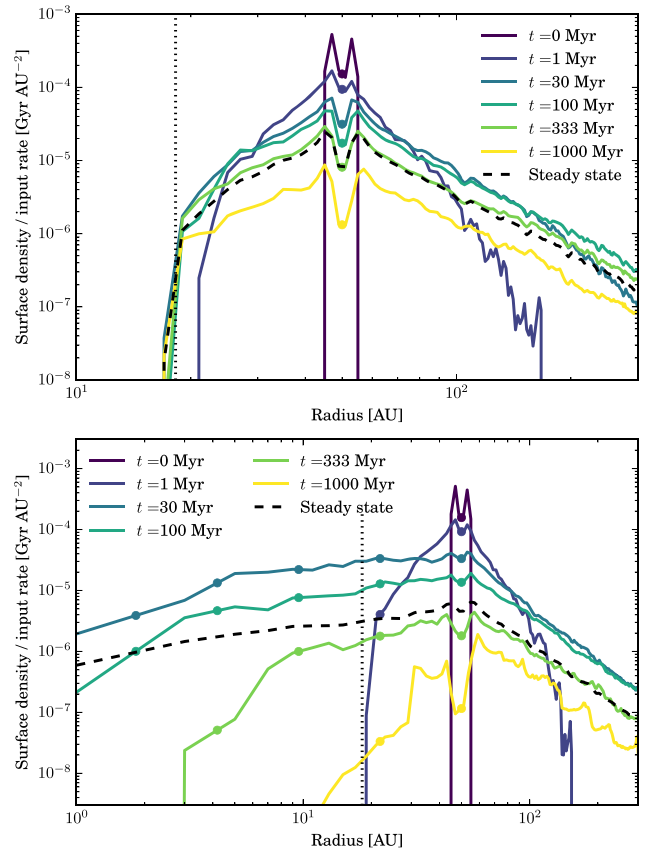


**Figure 4.** Surface density of particles as a function of time (colours) for the scenario in which particles start at  $t = 0$  in the chaotic zone of a planet at 50 au in the single planet case (top) and in our reference multiplanet system (bottom). The black dashed line represents the steady-state surface density when particles are input in the system at a constant rate in the chaotic zone of the outermost planet. The radial location of the dots corresponds to the semimajor axis of each planet. The black dotted vertical line represents  $q_{\min, p1}$ . At  $t = 0$  the distribution of particles is double peaked near 50 au because we removed those particles that stayed as Trojans. Note that the  $x$ -axis in the lower panel extends further in than in the upper panel.

steeply with orbital radius  $\propto r^{-\gamma}$ , where  $\gamma$  is about  $-3$  as expected for a scattered disc population with a common pericentre (Duncan et al. 1987). Within 50 au  $\Sigma(r)$  decreases towards smaller orbital radii, but with a sharp edge at 18 au, which is the location of  $q_{\min, p1}$ , expected since no particles should be scattered interior to this.

### 5.2 Reference system

When considering our reference chain of equal mass  $30 M_{\oplus}$  planets separated by 20 mutual Hill radii, we find that the fraction of particles that are ejected increases relative to the single planet case from 85 to 93 per cent, with a shorter ejection time-scale of 120 Myr (compared with 380 Myr in the single planet case). The shorter ejection time-scale is due to multiple scattering with interior planets as well as the outermost planet, which makes particles evolve faster on to unbound orbits. After 1 Gyr of evolution, only 5 per cent remain in the system, most of which are in a scattered disc beyond 50 au (see yellow line on the bottom panel of Fig. 4). As predicted, the presence of multiple planets makes it easier for particles to be scattered inwards, and the fraction of particles that cross 0.5 au increases from  $<0.65$  to  $3.7^{+0.9}_{-0.7}$  per cent. On the other hand, the

fraction of particles that are accreted by planets decreases relative to the single planet case from 15 to 3.6 per cent (0.4 per cent by inner planets). This is because particles are scattered by multiple planets, thus increasing the level of stirring and reducing the number of close encounters that they have with the outermost planet (e.g. the steady-state surface density near the outermost planet is lower by a factor of 2 in the reference system).

The bottom panel of Fig. 4 shows the evolution of  $\Sigma(r, t)$  and its steady-state form when particles are input at a constant rate. Beyond 50 au, the system has a surface density similar to the single planet case, but within 50 au it is flatter and extends within  $q_{\min, p1}$  as particles are scattered by inner planets. Within 10 au,  $\Sigma(r)$  approximates to a power law with a slope of  $\sim 0.7$ , which flattens out towards 50 au. This slope is overall steeper compared to the surface density expected in a P-R drag scenario (van Lieshout et al. 2014; Kennedy & Piette 2015); thus, if material was detected between an outer belt and exozodi, the slope could be used to discern between scattering and P-R drag scenarios. Note that the surface density within a few AU could be underestimated due to our boundary condition at 0.5 au. Particles within a few AU are likely to be highly eccentric after being scattered multiple times, with pericentres that could reach 0.5 au, and thus, be removed from the simulation. This is investigated further in Section 6.6 decreasing our inner boundary to 0.1 au. The short lifetime of particles in the system with multiple planets is also manifested in the surface density at  $t = 1$  Gyr that is significantly lower compared to the single-planet system. It is also worth noting that whereas Fig. 4 shows the evolution of the surface density, future figures will only show the steady-state surface density.

### 5.3 Varying $K(a)$

Here we present results from four simulations of equal mass planets ( $30 M_{\oplus}$ ), but with different spacings, measured with the number of mutual Hill radii ( $K$ ) between adjacent planets. These are planet configurations 4, 5, 8, 9, and 11, for which  $\alpha_{\Delta}$  and  $K_0$  vary (see Fig. 3 upper and lower right panels). We also include results from the reference and single-planet system for comparison. Fig. 5 presents the results for  $\Sigma(r)$ ,  $f_{ej}$ ,  $t_{ej}$ ,  $f_{in}$ , and  $f_{acc, p}$ .

#### 5.3.1 Varying $K$ uniformly

When increasing the spacing from  $K = 20$  (reference system, dark blue, called mid  $K$  in Fig. 5) to 30 (yellow, high  $K$ ), we observe the following effects:

(i) The surface density of scattered particles is higher in the outer scattered disc, but much lower towards smaller orbital radii. In fact, the surface density is very similar to the single planet case beyond  $q_{\min, p1}$ . Only a very small fraction extends within 18 au as expected because the next planet in the chain is inside  $q_{\min, p1}$ .

(ii) The fraction of ejected particles is 87 per cent, slightly lower than the 93 per cent in our reference system and similar to the single planet case. This difference is due to the higher fraction of accreted particles (12 per cent by the outermost planet).

(iii) The ejection time-scale is also increased from 120 to 404 Myr. The longer lifetime of particles causes the surface density to be higher beyond 50 au in the case of large planet spacing. In fact, both  $f_{ej}$  and  $t_{ej}$  are very similar compared to the single planet case. The rest of the particles that are not ejected are mostly accreted by the outermost planet (12 per cent).

(iv) Only a very small fraction of particles are able to cross 0.5 au (1.4 per cent).

(v) The fraction accreted per inner planet is zero, but statistically consistent with the results of our reference system ( $\lesssim 0.65$  per cent). This is because there is only one planet within 10 au in this system, therefore there is a large uncertainty on  $f_{acc, p}$ .

(vi) After 1 Gyr of evolution, 14 per cent of particles remain in the scattered disc beyond the outermost planet.

Therefore, we find that when increasing the spacing, the results approximate to the single planet case, with the subtle difference that a few particles are able to be scattered within  $q_{\min, p1}$ . These results confirm the first prediction that planet configurations with outer planets too widely spaced, i.e. with  $a_{p2} < q_{\min, p1}$ , would be inefficient at scattering particles inwards as multiple scattering is hindered.

When  $K$  is lower, e.g. 12 or 8 (represented with light blue colours) instead of 20, we observe the following effects:

(i) The surface density of the scattered disc is lower at both small and large orbital radii compared to our reference planet configuration.

(ii) On the other hand,  $f_{in}$  increases as the planet separation ( $K$ ) is decreased. This is because scattering by inner planets becomes more likely as particles do not require high eccentricities to reach the next planet in the chain. Therefore, inward scattering happens faster and before particles get a kick strong enough to be ejected from the system or get accreted by a planet. Note that although the amount of material being passed inwards is higher,  $\Sigma(r)$  is lower. This is because the steady-state surface density is also proportional to the lifetime of particles at a specific orbital radius. For example, at 10 au we find that  $\Sigma(r)$  is lower compared to the reference system by a factor that is consistent with the ratios of ejection time-scales (see Table 2), which is a proxy for the lifetime of particles in the scattered disc. We also rule out that the decrease in  $\Sigma(r)$  is due to the increase in  $f_{in}$ , as the removal of particles only has an effect within 4 au (see Appendix C).

(iii) We also find a decrease in the fraction of particles accreted per inner planet when the planet separation becomes low ( $K = 12$  and 8, light blue points in the lower right panel in Fig. 5). This effect is also observed in Section 5.4 at a significant level. This could be due to the lower surface density as the planet masses are the same. Other factors could be at play too, such as the eccentricity and inclination distribution of particles which can change the distribution of relative velocities in close encounters (equations 6 and 7). In fact, we do find that in systems with low spacing the distribution of eccentricities and inclinations is slightly shifted towards higher values by a few percent compared to the reference system, although this difference is not large enough to explain the lower accreted fraction. Therefore, we conclude that it is the change in surface density the main factor at decreasing the accretion on to planets. These results suggest that there is an optimum planet spacing that maximizes the accretion on to inner planets for systems of equal mass planets.

#### 5.3.2 Varying $K$ as a function of $a_p$ ( $\alpha_{\Delta}$ )

When the planet spacing decreases towards larger orbital radii (purple), the surface density remains very similar to our reference scenario, although slightly lower between 30 and 150 au. This simulation also has a similar or consistent fraction of particles that are accreted per inner planet and that cross 0.5 au compared to our reference case. On the other hand, the ejection time-scale in this simulation (79 Myr) is more similar to the low spacing case ( $K = 12$ ), which has outermost planets at similar separations. This suggests that the ejection time-scale is dominated by the separation

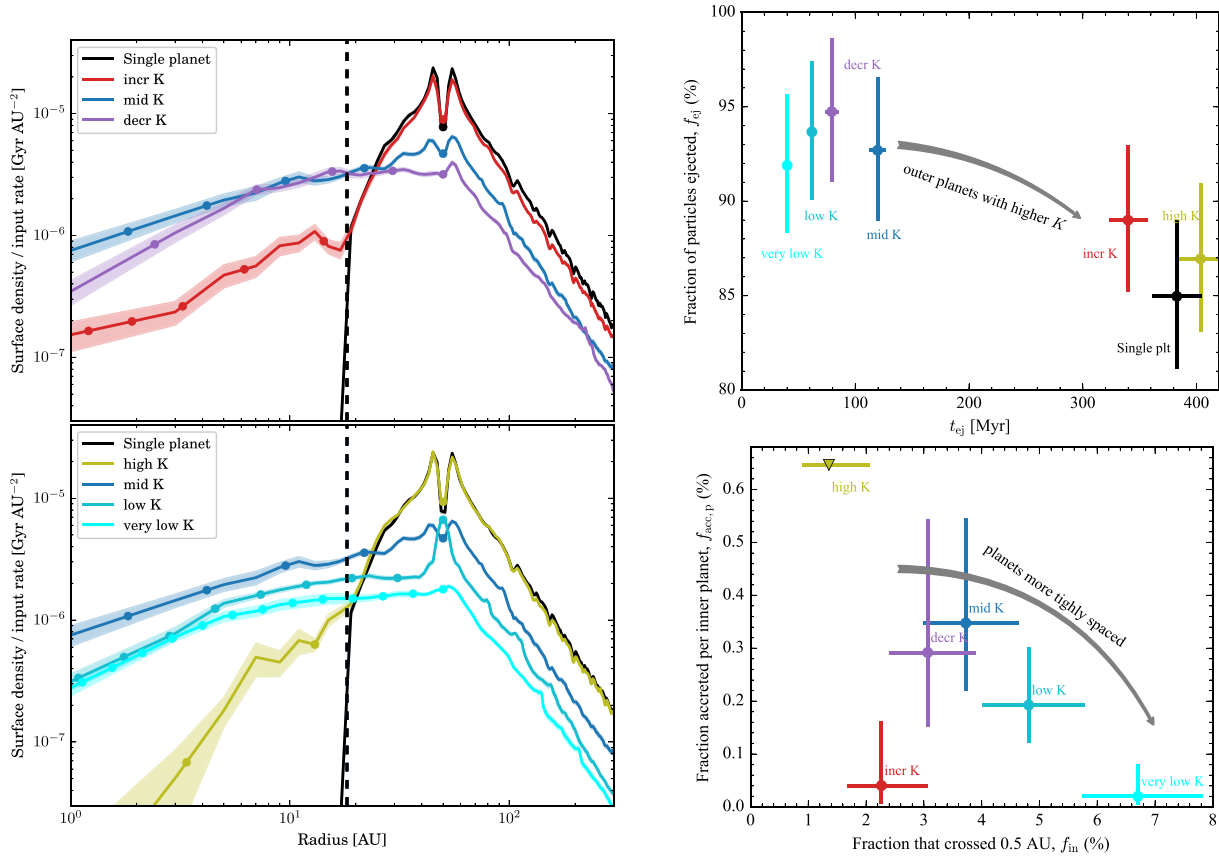


**Figure 5.** Results from  $N$ -body simulations for planet configurations with  $30 M_\oplus$  planets and varying the spacing between planets. *Left:* steady-state surface density distribution of particles. Models varying  $\alpha_\Delta$  are shown in the top left panel, while models with constant separations in mutual Hill radii of 8, 12, 20, and 30 in the bottom left. The radial location of the dots corresponds to the semimajor axis of each planet. Particles are input in the chaotic zone of the outermost planet at a constant rate. The black dashed vertical line represents  $q_{\min, p1}$ . The black continuous line represents the surface density of a single-planet system ( $a_p = 50$  au). *Top right:* fraction of particles ejected versus ejection time-scales, calculated as the median of epochs at which particles are ejected. *Lower right:* fraction of particles accreted per planet within 10 au versus fraction that crosses the inner boundary at 0.5 au.

**Table 2.** Results for each of the different planetary configurations. All the fractions are with respect to the total number of particles lost after 1 Gyr of simulation. The fraction of trojans is computed with respect to the total number of particles (1000). The uncertainties are estimated based on 68 per cent confidence intervals and assuming a Poisson distribution. The upper limits correspond to  $2\sigma$  (95 per cent confidence upper limit).

| Number | Label         | Colour     | $f_{ej}$ (per cent)  | $f_{in}$ (per cent) | $f_{acc}$ (per cent) | $f_{acc,p}$ (per cent) | Fraction accreted per planet (per cent)                           | Fraction remaining after 1 Gyr (per cent) | Absolute fraction of Trojans (per cent) | $t_{ej}$ (Myr) |
|--------|---------------|------------|----------------------|---------------------|----------------------|------------------------|---|---|---|----------------|
| 0      | single planet | black      | $85.0^{+4.0}_{-3.9}$ | <0.65               | $15.0^{+1.8}_{-1.6}$ | –                      | (15.0)  | $17.0^{+1.7}_{-1.6}$                      | $31.1^{+1.9}_{-1.8}$                    | $383 \pm 21.9$ |
| 1      | reference     | blue       | $92.7^{+3.9}_{-3.7}$ | $3.7^{+0.9}_{-0.7}$ | $3.6^{+0.9}_{-0.7}$  | $0.35^{+0.20}_{-0.13}$ | (0.3, 0.4, 0.3, 0.1, 2.4)   | $4.8^{+1.0}_{-0.8}$                       | $29.5^{+1.8}_{-1.7}$                    | $120 \pm 7.1$  |
| 2      | incr M        | orange     | $95.1^{+3.7}_{-3.5}$ | $2.9^{+0.8}_{-0.6}$ | $2.0^{+0.7}_{-0.5}$  | <0.15                  | (0.0, 0.0, 0.0, 0.0, 0.1, 1.8)                                    | $0.4^{+0.4}_{-0.2}$                       | $23.8^{+1.6}_{-1.5}$                    | $12 \pm 0.8$   |
| 3      | decr M        | green      | $92.3^{+4.4}_{-4.2}$ | $3.1^{+1.0}_{-0.8}$ | $4.6^{+1.2}_{-0.9}$  | $1.06^{+0.44}_{-0.31}$ | (0.8, 1.3, 1.2, 0.4, 1.0)   | $27.7^{+2.1}_{-2.0}$                      | $28.2^{+1.8}_{-1.7}$                    | $350 \pm 29.3$ |
| 4      | incr K        | red        | $89.0^{+4.0}_{-3.8}$ | $2.3^{+0.8}_{-0.6}$ | $8.7^{+1.4}_{-1.2}$  | $0.04^{+0.12}_{-0.03}$ | (0.0, 0.0, 0.2, 0.0, 0.3, 8.3)                                    | $11.2^{+1.4}_{-1.3}$                      | $30.4^{+1.8}_{-1.7}$                    | $340 \pm 16.8$ |
| 5      | decr K        | purple     | $94.7^{+3.9}_{-3.7}$ | $3.1^{+0.8}_{-0.7}$ | $2.2^{+0.7}_{-0.6}$  | $0.29^{+0.25}_{-0.14}$ | (0.3, 0.3, 0.3, 0.3, 1.0)   | $1.4^{+0.6}_{-0.4}$                       | $30.5^{+1.9}_{-1.7}$                    | $79 \pm 5.8$   |
| 6      | high M        | brown      | $94.8^{+3.7}_{-3.6}$ | $1.9^{+0.7}_{-0.5}$ | $3.3^{+0.8}_{-0.7}$  | $0.07^{+0.21}_{-0.06}$ | (0.1, 0.0, 0.1, 3.0)  | $0.4^{+0.4}_{-0.2}$                       | $26.6^{+1.7}_{-1.6}$                    | $28 \pm 1.3$   |
| 7      | low M         | pink       | $89.7^{+4.5}_{-4.3}$ | $4.5^{+1.2}_{-1.0}$ | $5.8^{+1.3}_{-1.1}$  | $0.45^{+0.19}_{-0.13}$ | (0.4, 0.4, 0.4, 0.8, 0.2, 0.6, 0.8, 2.1)                          | $30.4^{+2.2}_{-2.1}$                      | $30.5^{+1.9}_{-1.7}$                    | $583 \pm 36.2$ |
| 8      | high K        | yellow     | $86.9^{+4.0}_{-3.8}$ | $1.4^{+0.7}_{-0.5}$ | $11.7^{+1.6}_{-1.4}$ | <0.65                  | (0.0, 0.0, 11.7)  | $15.2^{+1.6}_{-1.5}$                      | $30.4^{+1.8}_{-1.7}$                    | $404 \pm 22.0$ |
| 9      | low K         | light blue | $93.7^{+3.7}_{-3.6}$ | $4.8^{+1.0}_{-0.8}$ | $1.5^{+0.6}_{-0.4}$  | $0.19^{+0.11}_{-0.07}$ | (0.3, 0.4, 0.1, 0.0, 0.1, 0.1, 0.4, 0.0, 0.0)                     | $1.5^{+0.6}_{-0.4}$                       | $26.2^{+1.7}_{-1.6}$                    | $62 \pm 4.2$   |
| 10     | low M - low K | grey       | $90.6^{+4.1}_{-3.9}$ | $7.3^{+1.3}_{-1.1}$ | $2.0^{+0.8}_{-0.6}$  | $0.12^{+0.09}_{-0.05}$ | (0.0, 0.0, 0.2, 0.0, 0.3, 0.2, 0.2, 0.2, 0.0, 0.2, 0.3, 0.5)      | $14.4^{+1.6}_{-1.4}$                      | $31.4^{+1.9}_{-1.8}$                    | $284 \pm 19.4$ |
| 11     | very low K    | light blue | $91.9^{+3.7}_{-3.6}$ | $6.7^{+1.1}_{-1.0}$ | $1.4^{+0.6}_{-0.4}$  | $0.02^{+0.06}_{-0.02}$ | (0.0, 0.0, 0.0, 0.0, 0.1, 0.0, 0.0, 0.0, 0.1, 0.1, 0.1, 0.4, 0.4) | $0.4^{+0.5}_{-0.2}$                       | $28.1^{+1.8}_{-1.7}$                    | $40 \pm 2.5$   |

of the two outermost planets rather than the average separation of planets in the system (for equal mass planets). However, despite the fact that the outer planets are close to each other, the fraction of particles that cross 0.5 au is lower or consistent with the reference system (dark blue).

In the system with increasing planet spacing (red), we find that the ejection time-scale and surface density beyond  $q_{\min, p1}$  are very similar to the case of high  $K$  (yellow) or the single planet case. As the spacing of the outermost planets increases scattering is dominated by the outermost planet. However, the surface density within  $q_{\min, p1}$

is much higher, as is the fraction of particles that get to 0.5 au compared to the high  $K$  and single-planet systems. The number of accreted particles per inner planet is lower compared to our reference system.

Neither increasing nor decreasing the spacing as a function of orbital radius increases the fraction of particles that get into the inner regions compared to our reference system. However, if we compare planet configurations with similar spacing for their outer planets (i.e. pairs yellow–red and light blue–purple), we find that if the planet spacing decreases towards smaller orbital radii, then the fraction of particles that cross 0.5 au and the surface density within  $q_{\min, p1}$  increases. Therefore, we predict that a system with both  $a_{p2} > q_{\min, p1}$  and  $\alpha_{\Delta} \geq 0$  will be very efficient at passing material inwards.

### 5.3.3 Conclusions regarding planet spacing

Therefore, based on these results we conclude the following:

- (i) For efficient inward multiple scattering, outer planets must be close enough such that  $a_{p2} > q_{\min, p1}$  – noting that  $q_{\min, p1}$  depends on the initial condition of particles which could be different to that assumed here.
- (ii) Closely spaced outer planets means that particles are ejected faster – assuming particles start in the outer regions of the system.
- (iii) Planets in compact configurations, with either uniform spacing or decreasing towards smaller orbital radii for a fixed outermost planet separation, are most efficient at passing particles inwards.
- (iv) The more closely packed the planets are, the lower the surface density in the scattered disc, and the fewer impacts per inner planet.

## 5.4 Varying $M_p(a)$

In this section, we present results from four other simulations of planets separated by 20 mutual Hill radii, but varying their masses. These are planet configurations 2, 3, 6, and 7, for which  $\alpha_M$  and  $M_0$  vary. We also include the reference system and configuration 10 which has low-mass planets closely spaced to see the effect of decreasing both planet masses and spacing. Fig. 6 presents the results for  $\Sigma(r)$ ,  $f_{ej}$ ,  $t_{ej}$ ,  $f_{in}$ , and  $f_{acc, p}$ .

### 5.4.1 Varying $M_p$ uniformly

Our simulations show that at constant separation ( $K$ ), the surface density, the ejection time-scale, and the fractions of particles that are accreted per inner planet and that cross the inner edge decrease when increasing planet mass (Fig. 6, see changes from pink to dark blue and from dark blue to brown). The ejection time-scale decreases in factors of  $\sim 4$ – $5$  when increasing  $M_p$  from 10 to  $30 M_{\oplus}$  and from 30 to  $90 M_{\oplus}$ , as higher mass planets scatter on shorter time-scales. Note that this factor is smaller than that predicted using equation (5) which could be due to the lower number of planets when increasing  $M_p$  (while keeping the spacing constant in mutual Hill radii). The change in ejection time-scale also results in the surface density increasing by similar factors when decreasing  $M_p$ . These strong differences in surface density cause also an increment in the fraction of particles accreted per inner planet when decreasing  $M_p$ . We also find that all inner planets accrete a similar fraction of particles in the system of low-mass planets (pink). While 31 per cent of particles remain in the system by 1 Gyr, when extending the integration to 5 Gyr we find that the fractions of particles ejected, accreted and that cross 0.5 au do not change significantly (see Section 6.6).

We can use these results to derive an empirical relation for the fraction of particles that get into 0.5 au and surface density as a function of the planet mass, for a fixed input rate and a chain of equal mass planets separated by 20 mutual Hill radii. We find that  $f_{in}$  varies approximately as  $M_p^{-0.37 \pm 0.13}$  and the surface density at 10 au as  $M_p^{-1.6 \pm 0.2}$ . This indicates that the surface density in the scattered disc is not directly proportional to the fraction of particles that get to 0.5 au, with the surface density being more sensitive to changes in planet mass. We can combine these two empirical expressions to find  $f_{in} \propto \Sigma(10 \text{ au})^{0.23 \pm 0.09}$  for chains of equal mass planets.

### 5.4.2 Varying $M_p$ as a function of $a_p$ ( $\alpha_M$ )

When varying  $\alpha_M$  with a fixed planet mass of  $30 M_{\oplus}$  at 10 au (see the top left panel of Fig. 3 and compare orange blue and green), we find the following. For planet masses decreasing with orbital radius ( $\alpha = -1$ ,  $M_{\text{green}}$ ), the ejection time-scale is increased relative to the reference system. Similarly, for planet masses increasing with orbital radius ( $\alpha = 1$ ,  $M_{\text{orange}}$ ), the ejection time-scale is decreased. The changes in the ejection time-scale are due to its strong dependence on the mass of the outermost planet as that is where particles are initiated. This is similar to what we found in Section 5.3 in which the ejection time-scale is dominated by the separation of the outermost planets.

We also find that the surface density changes significantly when varying  $\alpha_M$  (Fig. 6 top left panel). For planet masses decreasing with distance to the star (decr M, green), the surface density becomes steeper both inside and outside 50 au, with a slope of  $\sim 1.5$  within 50 au. This causes  $\Sigma(r)$  to be lower (higher) within (beyond) 10 au compared to our reference system. For planet masses increasing with distance to the star, the surface density is lower and flatter (incr M, orange). The steep slope within 4 au and the peak at 43 au seen in the orange line are due to our inner boundary (together with low number statistics) and particles trapped in the 5:4 mean motion resonance with the outermost planet, respectively. The slope of the surface density within 50 au depends strongly on  $\alpha_M$  because the lifetime of particles or ejection time-scale is a function of  $M_p$  and  $a_p$  (equation 5); hence, more negative  $\alpha_M$ 's will result in steeper positive slopes.

Regarding the efficiency of particles reaching 0.5 au ( $f_{in}$ ), the bottom right panel in Fig. 6 shows that this is slightly lower compared to the reference system for both  $\alpha_M = -1$  and 1 (decr M and incr M, respectively), but consistent within errors. However, when comparing systems with outermost planets of similar mass (green–pink and brown–orange), we find that positive  $\alpha_M$  results in a slightly higher fraction of particles reaching 0.5 au, while slightly lower for negative  $\alpha_M$ . This partially contradicts one of our predictions in Section 3, that chains of planets with mass decreasing with distance to the star (i.e. scattering time-scales increasing with distance) would be better at inward scattering than systems with mass increasing with distance. We expect that this is due to the system with planet masses decreasing with distance from the star (green) having inner planets in the ejection regime (see the discussion in Section 5.5).

We find that the fraction of particles accreted per inner planets is the highest in the system with planet masses decreasing with orbital radius (0.8 and 1.3 per cent for the planets at 2 and 7 au, respectively) compared to the other 11 simulated systems. This is surprising as it has one of the lowest surface densities within 10 au. On the contrary, no particles were accreted by inner planets in the system with

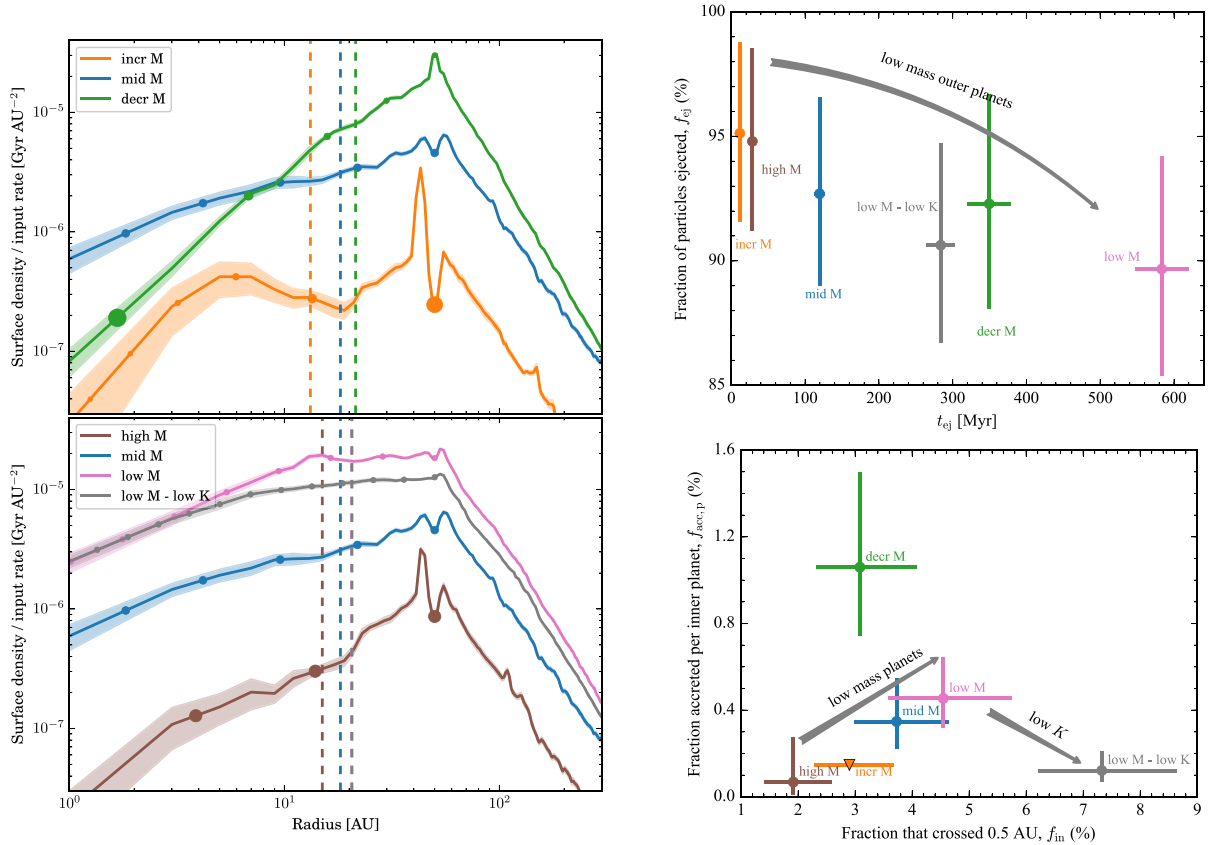


**Figure 6.** Results from  $N$ -body simulations for planet configurations with a constant planet spacing of 20 mutual Hill radii ( $K = 20$ ) and varying their masses. *Left:* steady-state surface density distribution of particles. Models varying  $\alpha_M$  are shown in the top left panel, while models with constant masses of 10, 30, and 90  $M_{\oplus}$  in the bottom left. The radial location of the dots corresponds to the semimajor axis of each planet and their size representing their masses with an arbitrary scale. Particles are input in the chaotic zone of the outermost planet at a constant rate. The dashed vertical lines represent  $q_{\min, p1}$ . *Top right:* fraction of particles ejected versus ejection time-scales, calculated as the median of epochs at which particles are ejected (lighter dots). *Lower right:* fraction of particles accreted per planet within 10 au versus fraction that crosses the inner boundary at 0.5 au. The inverted triangle represents a  $2\sigma$  upper limit. The grey line (lower left panel) and points (right panels) represent a system with 10  $M_{\oplus}$  planets closely separated by 12 mutual Hill radii.

planet masses increasing with orbital radius ( $f_{\text{acc}, p} \lesssim 0.15$  per cent). To understand what drives the higher accretion fraction per inner planet in the configuration with decreasing mass with orbital radius (green), we need to consider the density of particles around their orbits, the planet masses and radii, and the relative velocities of particles that the inner planets encounter (equation 6). As seen in Fig. 6 the surface density is not particularly high within 10 au compared, for example, to our reference configuration. Moreover, we analyse the number of close encounters per planet (those that get within 3 mutual Hill radii) finding that the surface density is a reasonable tracer of this quantity, being lower within 10 au. The higher level of accretion of the innermost planet for the simulation with decreasing mass with orbital radius (green) compared to the innermost planet in our reference simulation (dark blue) could be explained mostly by its higher planet mass (180 versus 30  $M_{\oplus}$ ) and radius. However, the second innermost planet also accretes significantly more than the inner planets in our reference system ( $\gtrsim 3$  times more), but with a slightly lower  $\Sigma(r)$  and a similar planet mass of 44  $M_{\oplus}$  and radius (remember that  $\Gamma$  is proportional to  $M_p^{4/3}$  for these planet masses and semimajor axes). Therefore, the fraction of accreted particles must be also enhanced by a difference in the distribution of eccentricities and inclinations of particles in these regions, which defines the relative velocities at which these planets are encountering scattered particles and the collisional cross-sections (see equation 7).

When comparing the distribution of eccentricities and inclinations of particles having close encounters, we find that their distributions are indeed significantly shifted towards lower values for the decr M system (see Fig. 7). Therefore, encounters happen on average at lower relative velocities and in a flatter scattered disc (lower  $h$ ). The lower eccentricities and inclinations, and higher collisional cross-section can increase  $R_{\text{acc}, \text{pl}t}$  by a factor of  $\sim 3$  for the second innermost planet of the decreasing mass system (green) compared to inner planets in our reference system, which is consistent with the higher number of impacts that we find for close-in planets. The lower eccentricities and inclinations are likely due to the fact that the outer planets scattering the material in from 50 au are lower in mass. We observe a similar effect for the system with equal low-mass planets (pink) and the opposite for the incr M system, i.e. higher eccentricities and inclinations are likely due to the high mass of the outermost planets.

#### 5.4.3 Low planet mass and spacing

Finally, in order to test if lowering the spacing of low-mass planets can increase even more  $f_{\text{in}}$  and possibly reduce  $f_{\text{acc}, p}$  as found in Section 5.3, in Fig. 6 we overlay a system with 10  $M_{\oplus}$  planets spaced with  $K = 12$  (grey). In accordance with our findings in Section 5.3, we find that such a system has a higher number

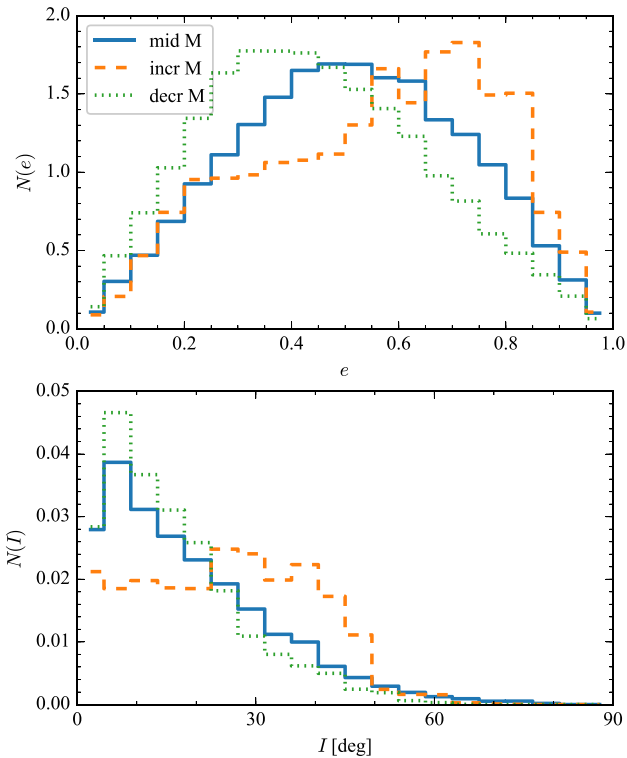


**Figure 7.** Normalized distribution of eccentricities and inclinations of particles having close encounters with planets within 10 au.

of particles that get to 0.5 au (7 per cent), but significantly lower  $f_{\text{acc}, p}$ . This is due to two effects: the surface density of the scattered disc is lower, but also we find that the distribution of eccentricities and inclinations in close encounters is shifted towards higher values. This suggests that there is an optimum separation ( $\gtrsim 12R_{H, m}$ ) that maximizes the amount of accretion per inner planet.

#### 5.4.4 Conclusions regarding planet masses

Therefore, based on the results varying the masses of the planets we conclude that:

- (i) The surface density decreases with increasing  $M_p$  for fixed planet spacing  $K$ .
- (ii) The slope of the surface density profile varies when varying the planet masses as a function of semimajor axis. For planet masses decreasing as a function of orbital radius,  $\Sigma(r)$  increases steeply with orbital radius compared to our reference system.
- (iii) The fraction of particles that get to 0.5 au increases when decreasing  $M_p$ . Placing the planets closer together increases even more the fraction of particles that get to 0.5 au, but reduces the surface density and thus the fraction of particles accreted per inner planet.
- (iv) Systems with innermost planets in the ejection regime are less efficient at transporting material within 0.5 au (green and brown).
- (v) The number of particles accreted per inner planet increases with decreasing  $M_p$  as the surface density is increased due to the longer lifetime of particles in the disc. However, systems with  $\alpha_M < 0$  have the highest  $f_{\text{acc}, p}$  because of the high collisional cross-section of inner planets caused by their high mass and planet

radii, and the low relative velocities of particles in the scattered disc.

#### 5.5 Comparison with our predictions

In this section we compare our results with previous work from which we made some predictions in Section 3.4. From analytic arguments three main results were expected. First, if particles start from a cold disc near the outermost planet, then systems with widely spaced planets, or at least with outermost planets too far from each other, would have trouble scattering particles inwards. In our simulations we find that this is approximately true, since systems with wide outer planets were the ones with the least amount of material transported to 0.5 au, confirming results by Bonsor et al. (2012).

The second expected outcome was that chains of high-mass planets will scatter and eject particles on shorter time-scales. In our simulations we find that this is true with ejection time-scales varying from 580 to 30 Myr when varying  $M_p$  from 10 to 90  $M_{\oplus}$ . Shorter ejection time-scales lead to lower surface densities of scattered particles.

The third expected outcome regarded the mass distribution of the planets in the chain, with the best systems passing material inwards being the ones with equal mass chain of planets or decreasing with distance from the star (Wyatt et al. 2017). We find that this is true for systems of equal mass planets, being the best of the simulated systems at scattering material inwards to within 0.5 au. Systems with decreasing mass were not as efficient at passing material inwards as they encounter the following problem. The outermost planet must have a mass high enough that the scattering time-scale is shorter than 1 Gyr (length of simulation), otherwise particles will take too long to be scattered inwards. This means that if the outermost planet is at 50 au, then it must be more massive than  $\sim 10 M_{\oplus}$  for a Gyr old system. However, if the planet masses increase towards smaller orbital radii, then the innermost planet at 1 au will be in the ejected region (see Fig. 3), hence ejecting most of the particles instead of scattering them in so that they can reach 0.5 au. This is similar to the Solar system where Jupiter ejects most of the minor bodies that are scattered in from the Kuiper belt, which thus never get into the inner Solar system.

The fourth expected outcome was that the accretion on to inner planets (which has implications for the delivery of volatile-rich material formed in an outer belt) will be higher if they are more massive, the surface density of particles around their orbits is higher, and particles are on low eccentricity and inclination orbits. We confirmed this, however, as expected we also found that these factors are not independent of each other as the planet mass and spacing affect both the surface density and the distributions of eccentricity and inclination of scattered particles. We found that systems of low-mass planets have the highest accretion per inner planet as the density of particles is highest for these systems. If planet masses are allowed to vary as a function of orbital radius, we find that the system with low-mass outer planets and high-mass inner planets has the highest accretion per inner planet, as it is an optimum of the different factors presented above confirming our predictions. Finally, we also found that there must be an optimum planet separation for delivering material to inner planets. While particles in systems with planets widely spaced are less likely to be scattered inwards, particles in systems of tightly packed planets are ejected on shorter time-scales and have higher relative velocities, hence both wide and small planet spacing hinder accretion on to inner planets.

## 6 DISCUSSION

In this paper, we have explored the process of inward scattering for a variety of planetary systems. Below we discuss our main findings regarding the surface density of scattered particles, inward transport to 0.5 au, and delivering material to inner planets. We also discuss some of our model assumptions and simulation parameters.

### 6.1 Can we detect the scattered discs in a system with an exozodi?

Consider a system that is observed to have an exozodi. IR observations of the dust emission can be used to infer the rate at which mass is lost from the exozodi,  $R_{\text{zodi}}$ . For example, for  $\sim 1$  Gyr old systems with exozodis such as Vega,  $\eta$  Corvi, and HD69830 this is  $R_{\text{zodi}} \sim (10^{-11})\text{--}(10^{-9}) M_{\oplus} \text{ yr}^{-1}$  (see equation 29 in Wyatt et al. 2007a), being highest for Vega and  $\eta$  Corvi. Here we consider what constraints the results from Section 5 place on the possibility that an exozodi is replenished by scattering of planetesimals from an outer belt. The two conditions that we must consider are whether mass is passed in at a sufficient rate to replenish the exozodi at a rate  $R_{\text{zodi}}$  and whether this requires the presence of a scattered disc between the outer disc and the exozodi that is bright enough to be detectable. Below we first present some general considerations to estimate the surface density of dust in the disc of scattered particles to compare it with sensitivity limits from different telescopes (Section 6.1.1). Then we apply these to a specific system (Section 6.1.2).

#### 6.1.1 General considerations

As discussed in Section 2, here we assume that solids from an outer belt of planetesimals are input near an outermost planet (located at 50 au) at a constant rate  $R_{\text{in}}$ , and that when they cross 0.5 au their mass is incorporated in a collisional cascade where solids are ground down to dust. Then  $R_{\text{zodi}} = f_{\text{in}} R_{\text{in}}$ , and if we assume that scattering has been ongoing for the system's whole lifetime, the total mass that has been scattered from the outer belt is  $t_{\star} R_{\text{zodi}} / f_{\text{in}}$ , where  $t_{\star}$  is the age of the system. It is worth noting that although  $f_{\text{in}}$  varies as a function of the planetary system architecture, it does not change by more than an order of magnitude when varying considerably the planet masses and spacing (based on our simulations,  $f_{\text{in}}$  is in the range 1–7 per cent). This means that for  $\sim 1$  Gyr old systems with a high  $R_{\text{zodi}}$  of  $\sim 10^{-9} M_{\oplus} \text{ yr}^{-1}$  (e.g. Vega or  $\eta$  Corvi) the amount of material scattered from the outer belt over the lifetime of the system (assuming this is the origin of the exozodi) is probably as high as  $\sim 10 M_{\oplus}$  if this has been a continuous process or even higher if not all of the mass that reaches 0.5 au ends up in the exozodi. Note that this is a significant fraction of estimated masses of their outer belts assuming a size distribution with a power index of  $-3.5$  and a maximum planetesimal size of 10–100 km (Holland et al. 2017; Marino et al. 2017a).

Comparing the fraction of particles that get to 0.5 au with the surface density of particles (Fig. 8), we find that there is a correlation between the two. This correlation is similar to the one that we found in Section 5.4.1, with  $f \propto \Sigma(10 \text{ au})^{0.23 \pm 0.09}$ . That is, while the surface density varies by two orders of magnitude,  $f_{\text{in}}$  only varies by a factor of a few. Moreover, although there is a correlation for systems with equal planet spacing ( $K = 20$ ) and different planet masses (high M, reference and low M), there is an important dispersion for the rest of the architectures explored. This means that bright exozodis (i.e. high  $f_{\text{in}}$ ) do not necessarily require a bright scattered disc between the exozodi and outer belts [i.e. large  $\Sigma(10 \text{ au})$ ] if,

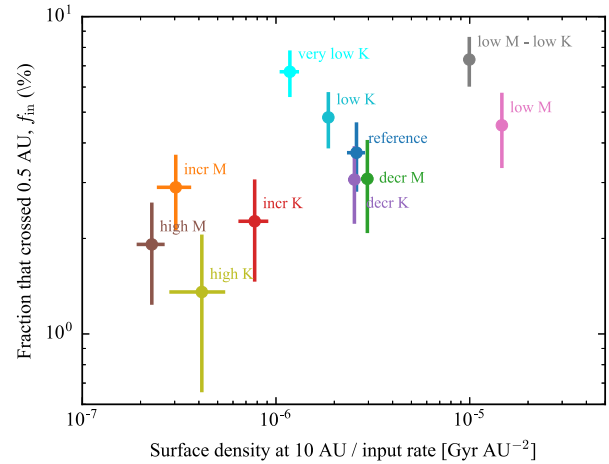


**Figure 8.** Fraction of particles that cross 0.5 au versus mass surface density at 10 au divided by the mass input rate for the simulated systems presented in Table 1.

for example, massive planets or tightly packed medium mass planets are present. Therefore, for a given exozodi, upper limits on the amount of material between these regions can help us to constrain the mass and separations of intervening planets (see Section 6.1.2).

To estimate if the scattered disc between the outer belt and the exozodi could be detected, we assume that the distribution of mass shown in Figs 5 and 6 is also a representative of the distribution of dust (i.e. neglecting radiation forces acting on small grains). Although collisions can deplete dust densities through collisions before being lost from the system (ejected, accreted, or transported within 0.5 au), dust should also be replenished by collisions of bigger bodies that are also scattered and have lifetimes longer than the scattering time-scales. We first obtain the total surface density of solids by scaling the surface density to the necessary input rate ( $R_{\text{in}}$ ) that can sustain a given exozodi ( $R_{\text{zodi}} = f_{\text{in}} R_{\text{in}}$ ). Then, we scale the surface density of solids to consider only the mass in dust grains smaller than 1 cm (as IR observations at wavelengths shorter than 1 mm are only sensitive to emission from dust grains smaller than  $\sim 1$  cm). In the scenario that we are considering solids originate in an outer debris belt, thus we assume a standard  $-3.5$  power-law size distribution of solids with a maximum size of 100 km and a minimum size of  $1 \mu\text{m}$ , roughly the blow-out size for a Sun-like star. Then the scaling factor to transform the total mass into the mass of dust grains smaller than 1 cm is  $\sim 3 \times 10^{-4}$ . This factor is approximately the same when using the resulting size distribution of solids at 50 au after 1 Gyr of evolution, and taking into account a size-dependent disruption threshold of solids (see the middle panel of fig. 9 in Marino et al. 2017b).

In Fig. 9 we show the predicted mass surface density of dust smaller than 1 cm for a system inferred to have  $R_{\text{zodi}} = 10^{-9}$  and  $10^{-11} M_{\oplus} \text{ yr}^{-1}$ , assuming these exozodis are fed by our reference chain of planets ( $f_{\text{in}} = 3.7$  per cent). The resulting surface densities are  $\sim (10^{-8})\text{--}(10^{-10}) M_{\oplus} \text{ au}^{-2}$  within 50 au. Fig. 9 also compares these with typical sensitivities ( $3\sigma$  for 1 h observations) of ALMA at  $880 \mu\text{m}$  (0.1 mJy and 1 arcsec resolution), *Herschel* at  $70 \mu\text{m}$  (3.0 mJy and  $5''.6$  resolution), *JWST* at  $20 \mu\text{m}$  (8.6  $\mu\text{Jy}$  and 1 arcsec resolution), and a possible future 3-m far-IR (FIR) space telescope similar to SPICA at  $47 \mu\text{m}$  (15  $\mu\text{Jy}$  and  $3''.4$  resolution). We assume a system at a distance of 10 pc with a  $1 L_{\odot}$  central star. To translate the above sensitivities to dust masses, we assume blackbody temperatures and dust opacities corresponding to dust grains with a

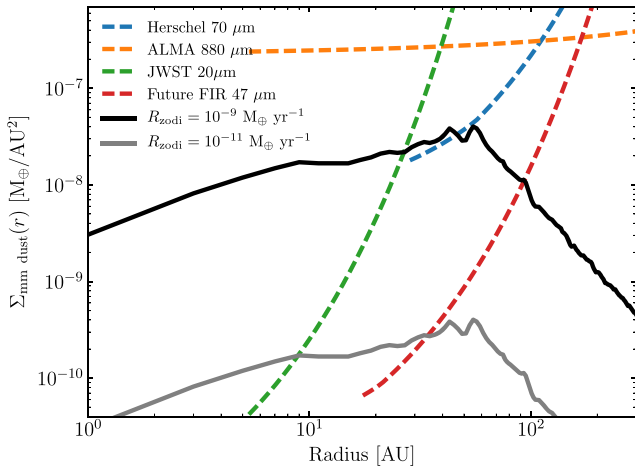


**Figure 9.** Steady-state surface density distribution of dust grains smaller than 1 cm for our reference system. The dashed lines represent the 1  $\sigma$  integration sensitivities ( $3\sigma$ ) from different instruments, assuming a distance of 10 pc, a face-on disc orientation, and azimuthally averaging the emission over 10 au wide annuli. The estimated sensitivities only extend inwards to half of the resolution. Note that for the ALMA sensitivity we have not considered the size of its primary beam as this can be overcome by multiple pointings (mosaic mode).

–3.5 size distribution and composed of a mix of amorphous carbon, astrosilicates, and water ice (e.g. Marino et al. 2017b). Moreover, assuming a face-on disc orientation sensitivities are also improved by azimuthally averaging the emission over 10 au (1 arcsec) wide disc annuli. Fig. 9 shows that although ALMA has one of the highest resolutions, it is not very sensitive to the dust emission within an outer belt at  $\sim 50$  au. *JWST* is more sensitive than ALMA within  $\sim 30$  au where dust is expected to be warmer and therefore emits significantly more at mid-IR wavelengths. In the FIR *Herschel* does better than ALMA within  $\sim 100$  au and could detect the scattered disc in systems with extreme exozodis; however, it is limited by its low resolution. A future FIR mission could do much better, being able to detect much fainter emission at 47  $\mu\text{m}$  and resolve structure down to 20 au. We conclude that current or previous instruments like ALMA or *Herschel* could only constrain the architecture of systems with the highest mass-loss rates (see the example below).

### 6.1.2 $\eta$ Corvi

$\eta$  Corvi is one of the best studied systems with hot/warm dust ( $\sim 400$  K; Stenel & Backman 1991; Smith et al. 2009). Its hot component has a fractional luminosity of  $\sim 3 \times 10^{-4}$  and its location was constrained to be between  $\sim 0.2$  and 1.4 au (Defrère et al. 2015; Kennedy et al. 2015; Lebreton et al. 2016). This implies that it can only be explained if material is resupplied from further out (e.g. an outer belt of planetesimals) at a rate of  $\sim 10^{-9} M_{\oplus} \text{ yr}^{-1}$  (Wyatt et al. 2007a). In fact, this system is known to host a massive cold debris disc located at around 150 au and resolved in the sub-millimetre and FIR (Wyatt et al. 2005; Duchêne et al. 2014; Marino et al. 2017a). Despite the presence of this massive outer belt which could feed an exozodi through small dust migrating due to P-R drag, this scenario has been discarded as an explanation for the large exozodi levels observed since it is not efficient enough (Kennedy & Piette 2015). Moreover, observations found no dust located between its hot and cold components. However, Marino et al. (2017a) did find evidence for CO gas at  $\sim 20$  au using ALMA observations. The

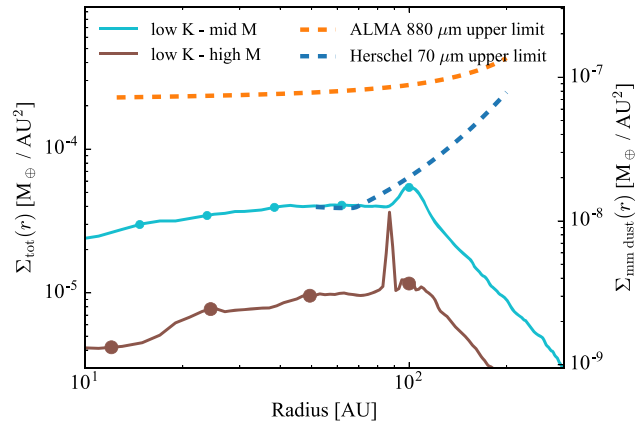


**Figure 10.** Steady-state surface density distribution of particles for a model tailored to  $\eta$  Corvi. Particles are input in the chaotic zone of the outermost planet ( $a_{p1} = 100$  au) at a constant rate of  $10^{-9}/f_{\text{in}} M_{\oplus} \text{ yr}^{-1}$ . All planets are spaced with  $K = 12$  and have masses of 30 (light blue) and 90  $M_{\oplus}$  (brown). The dashed lines represent the upper limits on the amount of mm-sized dust from ALMA at 0.88 mm (blue) and *Herschel* at 70  $\mu\text{m}$  (orange).

short-lived CO gas hints at the possibility of volatile-rich material being passed inwards from the outer belt and outgassing, consistent with spectroscopic features of the hot dust (Lisse et al. 2012). An outstanding question though is whether this can be achieved without requiring scattered disc densities that exceed the detection limits of FIR and sub-millimetre observations.

We run two new models with 30 and 90  $M_{\oplus}$  planets spaced with  $K = 12$  (tightly packed) to achieve a high inward scattering efficiency, but now extending the chain of planets up to 100 au – the maximum semimajor axis of a planet sculpting the inner edge of the outer belt (Marino et al. 2017a). In the first case, when extending the chain up to 100 au we find that  $f_{\text{in}}$  decreases from 4.8 to 2.8 per cent,  $t_{\text{ej}}$  increases from 62 to 120 Myr, and  $f_{\text{ej}}$  increases from 94 to 97 per cent. For the more massive planets, we find  $f_{\text{in}} = 2.1$  per cent,  $t_{\text{ej}} = 20$  Myr, and  $f_{\text{ej}} = 97$  per cent. We compute the expected total surface density for a mass input rate such that  $R_{\text{zodi}} = 10^{-9} M_{\oplus} \text{ yr}^{-1}$ . Under the same assumption stated in the previous section, we extrapolate  $\Sigma(r)$  to the surface density of dust grains smaller than 1 cm ( $\Sigma_{\text{mm dust}}$ ) assuming a –3.5 size distribution between the largest planetesimals and the cm-sized grains and an opacity of  $1.7 \text{ cm}^2 \text{ g}^{-1}$  at 880  $\mu\text{m}$ . However, given the existing constraints from image and spectral energy distribution modelling, we adopt a grain opacity index  $\beta = 0.2$  (i.e. an  $\sim -3.1$  grain size distribution) between FIR and sub-mm wavelengths. We also assume a dust temperature of 50 K at 100 au which increases towards smaller orbital radii as  $r^{-0.5}$ , consistent with radiative transfer modelling of this system. In Fig. 10 we compare  $\Sigma_{\text{mm dust}}$  from our simulations with the upper limits from ALMA and *Herschel* observations (Duchêne et al. 2014; Marino et al. 2017a). We find that for both types of systems, the sensitivity curves of ALMA and *Herschel* are above the predicted surface densities. The surface density of a 30  $M_{\oplus}$  chain barely reaches the  $3\sigma$  limit imposed by *Herschel*. The total mass in dust smaller than 1 cm in the scattered disc within 80 au is  $3 \times 10^{-4}$  and  $9 \times 10^{-5} M_{\oplus}$  for the systems with 30 and 90  $M_{\oplus}$  planets, respectively. These dust masses are well below the mass upper limit of  $2.7 \times 10^{-3} M_{\oplus}$  from ALMA observations (Marino et al. 2017a).

We can also compare these dust densities with alternative scenarios such as the P-R drag scenario. Although it is not efficient enough to explain  $\eta$  Corvi’s exozodi, P-R drag is inevitable and small dust will be dragged inwards and be present in between its exozodi and

outer belt with a surface density distribution close to flat. We find that the two simulated systems presented in this section have optical depths of  $(10^{-6})$ – $(10^{-5})$ , estimated as the product of the surface density and a standard dust opacity at optical wavelengths (assuming a  $-3.5$  grain size distribution with a minimum and maximum size of  $1 \mu\text{m}$  and  $1 \text{cm}$ , respectively). These optical depths are similar or slightly greater than for small dust migrating in due to P-R drag in the absence of planets (see fig. 1 in Kennedy & Piette 2015). Therefore, it is worth noting that observations looking for an intermediate component within a few AU in between bright exozodi and outer belts (e.g. using the Large Binocular Telescope Interferometer) should consider the possibility that any detected emission could correspond to a scattered disc rather than P-R dragged dust. Constraints on the radial profile of the surface density of dust could help to disentangle between these two scenarios as a scattered disc could have a steeper slope.

Now, we can go one step further and use our results to constrain the planet masses assuming that the exozodi in  $\eta$  Corvi is fed by scattering within a chain of equal mass planets. In Section 5.4.1, we found that in systems of equal mass planets and uniform spacing (20 mutual Hill radii) the surface density scales with planet mass approximately as  $M_p^{-1.6 \pm 0.2}$ , while the fraction of particles that get to  $0.5 \text{ au}$  scales as  $M_p^{-0.37 \pm 0.13}$ . Assuming these relations stay the same for planet chains out to  $100 \text{ au}$  and with low spacing (12 mutual Hill radii), we can approximate  $f_{\text{in}}$  and the surface density of dust smaller than  $1 \text{ cm}$  at  $60 \text{ au}$  ( $\Sigma_{\text{mm}, 60\text{au}}$ ) by

$$f_{\text{in}} = 0.028 \left( \frac{M_p}{30 M_{\oplus}} \right)^{-0.37}, \quad (13)$$

$$\Sigma_{\text{mm}, 60\text{au}} = 1.3 \times 10^{-8} \left( \frac{M_p}{30 M_{\oplus}} \right)^{-1.6} \left( \frac{R_{\text{in}}}{40 M_{\oplus} \text{Gyr}^{-1}} \right) M_{\oplus} \text{au}^{-2}, \quad (14)$$

where we have assumed a maximum planetesimal size of  $100 \text{ km}$  and fixed the values of  $f_{\text{in}}$  and  $\Sigma_{\text{mm}, 60\text{au}}$  to the ones presented above, only valid for chains of equal mass  $30 M_{\oplus}$  planets spaced by 12 mutual Hill radii. By equating equation (14) to the Herschel upper limit of  $1.3 \times 10^{-8} M_{\oplus} \text{au}^{-2}$  at  $60 \text{ au}$ , we can infer a maximum planet mass as a function of the mass input rate (orange solid line in Fig. 11). This limit assumes a maximum planetesimal size ( $D_{\text{max}}$ ) of  $100 \text{ km}$  and a  $-3.5$  power-law size distribution. A smaller  $D_{\text{max}}$  would make  $\Sigma_{\text{mm}, 60\text{au}}$  greater (dashed line), while a larger maximum planetesimal size would decrease the surface density of dust (dotted line). Larger planet spacing would also have an effect on the surface density, being increased for larger planet spacing as found in Section 5.3 (e.g.  $K = 20$ ).

We also expect that there is a limit on the mass input rate from an outer belt if it has been ongoing for  $1$ – $2 \text{ Gyr}$  (the age of  $\eta$  Corvi) at a constant rate. This limit is chosen such that the total mass scattered from the outer regions is  $\lesssim 100 M_{\oplus}$  (close to the solid mass available in a protoplanetary disc at this location) which is equivalent to a rate of  $\lesssim 100 M_{\oplus} \text{Gyr}^{-1}$ . This upper limit for the mass input rate is represented as a red region in Fig. 11, although the exact value is uncertain. This upper limit sets a lower limit for the fraction of scattered particles that get to  $0.5 \text{ au}$  of  $\sim 1$  per cent to resupply the exozodi. A caveat in this argument is that it assumes that mass has been continuously scattered in over  $\sim 1 \text{ Gyr}$  at a steady state. However, this could be significantly different if ongoing only for a fraction of the age of the system or if stochastic processes are at play, making  $R_{\text{zodi}}$  vary significantly over short periods of time (e.g.

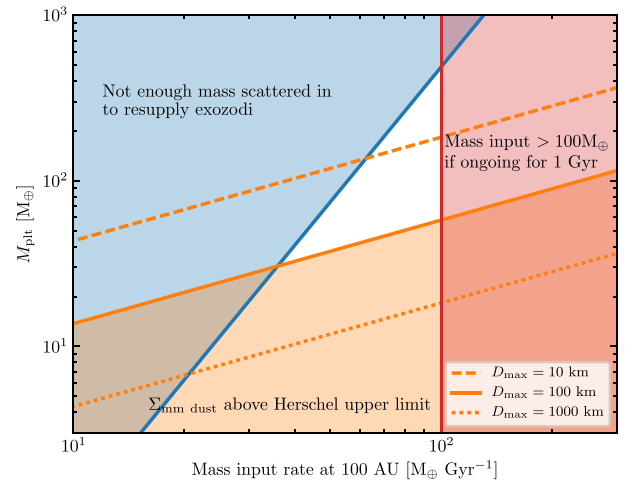


**Figure 11.** The planetary system that could orbit  $\eta$  Corvi and supply the exozodi, while not contradicting observational limits for the scattered disc, and assuming a constant mass input rate at  $100 \text{ au}$  and a system composed of equal mass tightly packed planets ( $K = 12$ ). The lower limit for the planet mass (orange) is estimated based on our result for the surface density as a function of the planet masses, the Herschel  $70 \mu\text{m}$  upper limit for dust between  $\eta$  Corvi’s outer belt and exozodi, and assuming a size distribution of solids up to a size of  $10$ ,  $100$ , and  $1000 \text{ km}$  (dashed, continuous, and dotted orange lines). The mass upper limit is estimated by setting the rate at which mass is transported into  $0.5 \text{ au}$  equal to the exozodi mass-loss rate. The red region is discarded as it would lead to unphysically large total solid mass beyond  $100 \text{ au}$  being scattered in for  $1$ – $2 \text{ Gyr}$ , although the exact upper limit for the mass input rate is uncertain. The white region represents the planet masses and mass input rate that are roughly consistent with the observational constraints and exozodi estimated mass-loss rate.

as explored in the context of white dwarf pollution; Wyatt et al. 2014).

In addition, because the fraction of particles that get to  $0.5 \text{ au}$  depends on the planet mass (equation 13), for a given mass input rate there is a maximum planet mass. This upper limit is represented as a blue region in Fig. 11 assuming chains of equal mass planets spaced by 12 mutual Hill radii. Planet chains with lower spacing would have a larger  $f_{\text{in}}$ , therefore the maximum mass could be pushed up, although planet chains with spacing smaller than  $10$  mutual Hill radii are likely to go unstable on  $\text{Gyr}$  time-scales. Wider planet spacing would result in a lower  $f_{\text{in}}$ , thus a smaller mass upper limit. It is important to note that these limits are conservative, as  $f_{\text{in}}$  is the maximum fraction of the material that could be incorporated into the exozodi, since some of that material that makes it to  $0.5 \text{ au}$  will end up being ejected, which would narrow the allowed white region in Fig. 11.

Based on these excluded regions, we can constrain the mass of the planets scattering material inwards and resupplying the exozodi. Assuming planets are of equal mass, spaced by 12 mutual Hill radii and a maximum planetesimal size of  $100 \text{ km}$ , we find that the mass input rate and planet mass must be greater than  $36 M_{\oplus} \text{Gyr}^{-1}$  and  $30 M_{\oplus}$ , respectively. If the maximum planetesimal size is larger (smaller), then the planet mass and mass input rate could be smaller (larger). In addition, assuming a maximum mass input rate of  $\sim 100 M_{\oplus} \text{Gyr}^{-1}$ , we find a maximum planet mass of  $300 M_{\oplus}$ . Planets much more massive than that are not efficient enough at scattering particles into  $0.5 \text{ au}$ . Future observations by *JWST* or FIR space missions could provide important constraints for the models explored here. A detection of dust between the outer belt and exozodi together with further modelling considering a wider variety of planetary system

architectures and P-R drag, could be used to constrain the planet masses in this planet scattering scenario.

### 6.2 Best system at transporting material within 0.5 au

We have found that the systems best suited for transporting material inwards are those with lower mass planets and that are tightly packed (at the limit of stability). Varying the planet spacing and mass as a function of orbital radius did not result in a higher fraction that reached 0.5 au. Moreover, although we varied to extremes the architecture of these planetary systems to study how the inward scattering efficiency changes, the fraction that reached 0.5 au did not change by more than a factor of  $\sim 7$ , while the surface density of the scattered disc varied by two orders of magnitude. This could imply that in order to explain the short-lived hot dust observed in many systems, no fine tuning is necessary, and a vast range of architectures could explain this frequent phenomenon.

Because in our analysis we assume that particles are immediately lost and converted into dust when crossing the inner boundary at 0.5 au; our results should be considered as an upper limit or as the maximum fraction of the mass scattered from the outer regions that could feed an exozodi assuming all the mass is processed into small dust with a 100 per cent efficiency. In reality, it is unlikely that all the mass scattered inside of 0.5 au will inevitably become the small dust that is observed as an exozodi. The exact mass fraction transformed into dust will depend on the specific mechanism that is at play and detailed modelling is needed. If dust is released by cometary activity, it would be necessary to consider the outgassing (e.g. Marboeuf, Bonsor & Augereau 2016) and disruption process of exocomets, together with the collisional evolution and radiation forces acting on dust grains. How fast the mass of a comet can be released in the form of dust via sublimation or disruption (spontaneous or due to tidal forces; Weissman 1980; Boehnhardt 2004) is uncertain; however, an order of magnitude estimate can be obtained from Jupiter-family comets (JFC) that have typical physical lifetimes of  $10^4$  yr (Levison & Duncan 1997). Hence, exocomets could disintegrate into small dust on time-scales much shorter than the scattering diffusion time-scale for the planet masses that we explored (equation 5 and Fig. 3). Therefore, removing particles immediately after they cross our inner boundary could be a reasonable approximation. Alternatively, the dust could arise from collisions of scattered planetesimals with an *in situ* planetesimal belt, although this may be inefficient if the collision probabilities are low.

### 6.3 Best system at delivering material to inner planets

We found that the best systems at delivering material to inner planets were those with low-mass outer planets and either with uniform mass or increasing towards smaller semimajor axis. This is a consequence of two factors. First, particles being scattered by low-mass planets can stay in the system for longer, increasing the density of particles near the planets, and so the probability of being accreted by a planet before being ejected. Secondly, particles scattered by lower mass planets tend to have lower eccentricities and inclinations, thus lower relative velocities, which increases the collisional cross-section of the planets. The latter is important as it also implies that the best systems at creating exozodis are not necessarily the best at delivering material to the inner planets (compare green, pink, and grey points in the bottom right panel of Fig. 6). For example, a system with low-mass tightly packed planets scatters twice the amount of particles into 0.5 au compared to our reference system, but with a similar fraction of accreted material per inner planet.

Similar to the fraction of material transported into 0.5 au, the efficiency of delivery to inner planets does not vary by more than an order of magnitude when comparing the different systems that we simulated. We find typical values between 0.1 to 1 per cent for the fraction of scattered particles that are accreted per inner planet. These could be even higher for lower mass planets (e.g. the Earth or super-Earths) if we extrapolate our results. Note that these fractions can be understood as collision probabilities, which are considerably higher than the  $10^{-6}$  collision probability of cometesimals with the Earth in the early Solar system (Levison et al. 2000; Morbidelli et al. 2000). It is unclear though how these results extrapolate to close-in planetary systems of chains of super-Earths, or close-in Earth-sized planets around low-mass stars (e.g. Trappist-1; Gillon et al. 2017). Most of these planets are in a different regime where they are much more likely to accrete particles rather than to eject them (Wyatt et al. 2017), and thus the accretion efficiencies and relative velocities could be very different (Kral et al. in preparation).

The low collision probability of comets has been used as an argument for the unlikely cometary origin for the water on the Earth. However, our results show that this conclusion cannot be simply extrapolated to extrasolar systems, as the low probabilities might be heavily determined by the presence of Jupiter and Saturn in the Solar system which eject most of the minor bodies that are scattered in from the outer regions never getting into the inner regions. We have shown that comet delivery can be much more efficient for other architectures and so could represent a significant source of water and volatiles for close in planets, although it is not clear yet how common are the architectures that we assumed in this paper. For example, assuming a total mass of  $1 M_{\oplus}$  of icy exocomets being scattered with an ice mass fraction of 0.5 dominated by water (roughly what is found in Solar system comets; see review by Mumma & Charnley 2011), the total amount of volatiles accreted could be higher than  $10^{-4} M_{\oplus}$  per inner planet, and if extrapolated to systems of  $1 M_{\oplus}$  planets, this could be enough to deliver the mass of the Earth's oceans and atmosphere ( $2 \times 10^{-4} M_{\oplus}$ ) to Earth-like planets.

An important caveat in our results regarding planet accretion is the uncertain fraction of volatiles (including water) that a planet is able to retain from an impact. This strongly depends on the impact velocities, mass of the planets, volatile fraction of planetesimals, presence of primordial atmospheres, and size of impactors (e.g. de Niem et al. 2012). These considerations are beyond the scope of this paper and require a statistical analysis of the impact velocities with a larger number of test particles than considered here.

### 6.4 Idealized planetary system

In this work we have considered idealized systems with regular or ascending/descending planet masses and spacings as a function of semimajor axis in order to test how scattering depends on planet properties. We do not know whether these idealized architectures really occur in nature, although some degree of regularity could be common (e.g. Millholland, Wang & Laughlin 2017; Weiss et al. 2018). Irregularities such as the presence of a very massive planet (e.g. ejector planet as described in Wyatt et al. 2017) in between a chain of lower mass planets (e.g. Jupiter and Saturn in the Solar system) could radically change the lifetime of particles and the probability of being scattered into the exozodi regions. Moreover, for certain planetary system architectures resonant effects may be important for scattering and could produce results that differ significantly from the trends that we found here. Therefore, further study is necessary to see how our results can be generalized over a broader range of architectures.

### 6.5 Migrating from exo-Kuiper belt to outermost planet

What could drive particles on stable orbits in the outer regions towards the outer planets? In this paper we have assumed this happens at a constant rate and for long time-scales. We now discuss possible mechanisms that could make these particles migrate in. For example, small dust in an outer debris belt could migrate in through P-R drag, encountering the outermost planet and being scattered further in by the chain of planets. However, this mechanism cannot produce a high mass input rate near the outermost planet as it only affects the small dust. Therefore, a mechanism arising from gravitational interactions affecting larger bodies is required. Particles could be slowly excited on to orbits with higher eccentricities and pericentres near the outermost planet by: chaotic diffusion produced by high-order or three-body resonances acting on long time-scales (Duncan, Levison & Budd 1995; Nesvorný & Roig 2001; Morbidelli 2005); secular resonances if multiple planets are present (Levison, Duncan & Wetherill 1994); mean-motion resonances with an exterior massive planet on a low eccentric orbit (Beust & Morbidelli 1996; Faramaz et al. 2017); dwarf planets embedded in the outer belt dynamically exciting smaller bodies (Muñoz-Gutiérrez et al. 2015); or Kozai oscillations induced by an outer companion. Alternatively, if the outer belt is massive enough the outermost planet could migrate outwards instead, while scattering material inwards and continually replenishing its chaotic zone (Bonsor et al. 2014). In these scenarios, particles that were initially near the outermost planet in the chain would start interacting with it with similar orbital parameters to those assumed here, thus we expect that the assumed initial conditions in this paper are representative of the scenarios stated above. A fourth possibility is that exocomets are fed from a massive exo-Oort cloud where they are perturbed by Galactic tides or stellar passages, decreasing their pericentres enough to have planet-crossing orbits (e.g. Veras & Evans 2013; Wyatt et al. 2017). In this last scenario, we expect that particles will start interacting with the planets at high eccentricities and inclinations, and the detailed origin might affect conclusions that rely on the Tisserand parameter (such as about the spacing of the outermost planets). All these scenarios could act on long-time-scales feeding material into the vicinity of the outermost planet in the chain. Although in this paper we have focused purely on the process of scattering (see Section 2), our results are independent of the rate at which these mechanisms can feed material into the vicinity of the outermost planet. Understanding how these different mechanisms can be coupled with the process of inward scattering by a chain of planets is the subject of future work.

### 6.6 Simulation parameters

Here we discuss the effect of changing some of the chosen simulation parameters. Throughout this paper we have assumed planets with a uniform bulk density of  $1.6 \text{ g cm}^{-3}$  (Neptune’s density), although planet densities could vary as a function of planet mass as suggested by Solar system and extrasolar planets (e.g. Chen & Kipping 2017, and references therein). For the range of planet masses used in this paper ( $4\text{--}180M_{\oplus}$ ), planet densities are expected to vary roughly as  $\sim M_p^{-0.8}$  (Chen & Kipping 2017), thus uniform density assumption could underestimate and overestimate the planet densities by a factor of 2.4 for 10 and  $90 M_{\oplus}$  planets, respectively. This translates to a factor of 1.3 in planet radius. For high-mass planets, the collisional cross-section is proportional to both mass and radius (due to gravitational focusing), thus the fraction of accreted particles could be underestimated by 30 per cent. On the other hand, the collisional cross-section of low-mass planets orbiting within 10

au could be either proportional to  $R_p^2$  (if the relative velocities are greater than the escape velocity) or  $R_p M_p$  (if gravitational focusing is important). Hence, the fraction of accreted particles could be overestimated by 25–45 per cent for low-mass planets. Therefore, the trend seen in 5.4.1 could become flatter if we considered densities varying as a function of planet mass.

We also tested the effect of changing some other parameters by varying the initial distribution of eccentricities and inclinations, extending the length of our simulations, and varying the inner boundary to shorter orbital radii. Depending on the specific mechanism inputting material near the outermost planet, particles will have different distributions of eccentricities and inclinations. When varying the initial eccentricity and inclination distributions in our reference system, we found that  $t_{ej}$ ,  $f_{in}$ ,  $f_{acc, p}$ , and  $\Sigma(r)$  do not change significantly, except when the eccentricities or inclinations are initially very high (e.g.  $e \gtrsim 0.2$ ; see details in Appendix A). Higher initial eccentricities led to slightly higher fractions of particles reaching 0.5 au and being accreted by inner planets. This could be due to a larger fraction of particles having a Tisserand parameter low enough to reach the second outermost planet.

To test if our results are robust against extending our simulations in time, we continued the simulation of low-mass planets (pink), which is the one with the slowest evolution, to 5 Gyr. We found that the new values of  $t_{ej}$ ,  $f_{in}$ ,  $f_{acc, p}$ , and  $\Sigma(r)$  are consistent with the ones obtained before (remember that these had been extrapolated to  $t = \infty$  on the assumption that the different outcomes occurred in the same proportions as they had up to 1 Gyr), confirming that 1 Gyr of simulation is enough to understand the behaviour of such systems (see details in Appendix B).

Finally, we moved our inner boundary from 0.5 to 0.1 au finding no significant changes in  $t_{ej}$ ,  $f_{acc, p}$ . As expected  $f_{in}$  is decreased and  $\Sigma(r)$  becomes flatter within 4 au as predicted in Section 5.2 (see details in Appendix C).

## 7 CONCLUSIONS

In this paper we have studied the evolution of exocomets in exoplanetary systems using a set of  $N$ -body simulations. We focused specifically on how the scattering process varies as a function of the architecture of the planetary system when exocomets originate in the outer region of a system (50 au), e.g. in an outer belt, and start being scattered in by the outermost planet. We are interested in the delivery of material to the terrestrial region, either as exozodiacal dust or cometary material (including volatiles) on to planets themselves.

This work aims to assess whether exocomets scattered by planets could provide a plausible explanation for exozodiacal dust commonly observed in exoplanetary systems. We find that the systems of tightly packed low-mass planets lead to the highest fraction ( $\sim 7$  per cent) of scattered comets reaching the inner regions, where they could resupply exozodis. Moreover, for a given pair of outermost planets, systems with decreasing (increasing) planet spacing and mass towards the star lead to higher (lower) levels of exozodis. We also find that systems with a very high mass innermost planet (e.g.  $150 M_{\oplus}$ ) are inefficient at producing exozodis. However, although tightly packed low-mass planets are the most efficient at feeding exozodis, the fraction of comets scattered within 0.5 au does not change by more than a factor of  $\sim 7$  (1–7 per cent) when varying the architecture of the planetary systems that we tested, noting that our simulations were generally devoid of planets more massive than  $0.3 M_{Jup}$ . The fact that this fraction does not

change by orders of magnitude suggests that many different types of planetary architectures could be efficient at feeding exozodis, possibly explaining the high frequency of exozodis around nearby stars.

In addition, we characterize the surface density of scattered comets between the exozodi region and an outer belt of exocomets. The surface density can be used as a test for the scattering scenario to resupply exozodis since feeding an exozodi could require the presence of a scattered disc that is bright enough to be detectable. First, we find that the surface density radial profile of the scattered disc between the planets typically increases with distance to the star instead of being flat as in a purely P-R drag scenario.

Secondly, unlike the fraction of scattered comets into 0.5 au ( $f_{in}$ ), the surface density of comets can vary by two orders of magnitude and is not directly proportional to the fraction scattered inwards. For example, systems of tightly packed planets have a higher  $f_{in}$ , but a lower surface density compared to a system of planets with medium spacing. This implies that for a given exozodi, the amount of scattered material present between the planets can vary depending on the specific planetary architecture, with systems of low-mass planets and medium spacing having the highest surface density of material between the planets. Future space missions like *JWST* or an FIR space telescope should be able to detect and characterize scattered discs in thermal emission around nearby systems with exozodis, setting tight constraints for the comet scattering scenario. For some systems, current observational limits already allow us to set some constraints. For example, the current Herschel and ALMA limits on the dust emission in between  $\eta$  Corvi's exozodi (<1 au) and outer belt (100–200 au) can be used to rule out some planetary architectures. For chains of equal mass planets and tightly spaced (12 mutual Hill radii), we find that only planet masses between 30 and 300  $M_{\oplus}$  could feed the exozodi at a high enough rate and hide an scattered disc below current upper limits, assuming the exozodi levels have stayed roughly constant and planetesimals/comets have a maximum size of about 100 km.

Finally, we have studied the delivery of volatiles by exocomets to the inner planets via impacts. We found that for a variety of architectures the delivery of material is relatively efficient. For every thousand comets scattered, between one and 10 are delivered to each inner planet. This is efficient enough to deliver the mass in the Earth's oceans if  $\sim 1 M_{\oplus}$  of icy exocomets were being scattered, which is reasonable considering the expected initial mass of exo-Kuiper belts. Of the planetary architectures explored in this paper, we found that chains of low-mass planets with medium spacing ( $\sim 20$  mutual Hill radii) are one of the most efficient at delivering comets to inner planets. If the spacing is reduced below  $\sim 20$  mutual Hill radii, the fraction of particles scattered to the exozodi region increases, but the number of impacts per inner planet decreases. This is because particles scattered by tightly spaced planets evolve faster and are lost before they can be accreted by a planet. This results in a lower surface density of the scattered disc for these systems. The systems that lead to the most planetary impacts have low-mass outer planets and high-mass inner planets. This configuration maximizes the collisional cross-section of inner planets as they have high masses and the particles scattered in by low-mass planets have lower relative velocities. Hence, low-mass outer planets are best suited for delivering material to the inner planets. Our results show that exoplanetary systems could potentially deliver volatiles to inner planets at a similar level to the Earth, and if chains of low-mass planets are common, they may not lack the volatiles necessary to sustain life.

## ACKNOWLEDGEMENTS

MCW and QK acknowledge funding from STFC via the Institute of Astronomy, Cambridge Consolidated Grant. AB acknowledges Royal Society via a Dorothy Hodgkin Fellowship.

## REFERENCES

- Absil O. et al., 2006, *A&A*, 452, 237  
 Absil O. et al., 2013, *A&A*, 555, A104  
 Beust H., Morbidelli A., 1996, *Icarus*, 120, 358  
 Boehnhardt H., 2004, in Festou M. C., Keller H. U., Weaver H. A., eds, Split Comets II, University of Arizona, Tucson. p. 301  
 Bonsor A., Wyatt M. C., 2012, *MNRAS*, 420, 2990  
 Bonsor A., Augereau J.-C., Thébaud P., 2012, *A&A*, 548, A104  
 Bonsor A., Raymond S. N., Augereau J.-C., 2013, *MNRAS*, 433, 2938  
 Bonsor A., Raymond S. N., Ormel C. W., 2014, *MNRAS*, 441, 2380  
 Booth M., Wyatt M. C., Morbidelli A., Moro-Martín A., Levison H. F., 2009, *MNRAS*, 399, 385  
 Brasser R., Duncan M. J., Levison H. F., 2008, *Icarus*, 196, 274  
 Carpenter J. M. et al., 2009, *ApJS*, 181, 197  
 Chambers J. E., 1999, *MNRAS*, 304, 793  
 Chambers J. E., Wetherill G. W., Boss A. P., 1996, *Icarus*, 119, 261  
 Chen J., Kipping D., 2017, *ApJ*, 834, 17  
 Cives S. et al., 2004, *Chem. Phys. Lett.*, 386, 169  
 de Niem D., Kürt E., Morbidelli A., Mutschmann U., 2012, *Icarus*, 221, 495  
 Debes J. H., Sigurdsson S., 2002, *ApJ*, 572, 556  
 Defrère D. et al., 2011, *A&A*, 534, A5  
 Defrère D. et al., 2015, *ApJ*, 799, 42  
 Dent W. R. F. et al., 2014, *Science*, 343, 1490  
 Dominik C., Decin G., 2003, *ApJ*, 598, 626  
 Duchêne G. et al., 2014, *ApJ*, 784, 148  
 Duncan M., Quinn T., Tremaine S., 1987, *AJ*, 94, 1330  
 Duncan M. J., Levison H. F., Budd S. M., 1995, *AJ*, 110, 3073  
 Eiroa C. et al., 2013, *A&A*, 555, A11  
 Ertel S. et al., 2014, *A&A*, 570, A128  
 Fang J., Margot J.-L., 2013, *ApJ*, 767, 115  
 Faramaz V., Ertel S., Booth M., Cuadra J., Simmonds C., 2017, *MNRAS*, 465, 2352  
 Farihi J., Barstow M. A., Redfield S., Dufour P., Hambly N. C., 2010, *MNRAS*, 404, 2123  
 Gänsicke B. T., Marsh T. R., Southworth J., Rebassa-Mansergas A., 2006, *Science*, 314, 1908  
 Gehrels N., 1986, *ApJ*, 303, 336  
 Geiler F., Krivov A. V., 2017, *MNRAS*, 468, 959  
 Gillon M. et al., 2017, *Nature*, 542, 456  
 Hillenbrand L. A. et al., 2008, *ApJ*, 677, 630  
 Holland W. S. et al., 2017, *MNRAS*, 470, 3606  
 Jackson A. P., Wyatt M. C., Bonsor A., Veras D., 2014, *MNRAS*, 440, 3757  
 Kennedy G. M. et al., 2015, *ApJS*, 216, 23  
 Kennedy G. M., Piette A., 2015, *MNRAS*, 449, 2304  
 Kennedy G. M., Wyatt M. C., 2013, *MNRAS*, 433, 2334  
 Kenyon S. J., Bromley B. C., 2008, *ApJS*, 179, 451  
 Koester D., Gänsicke B. T., Farihi J., 2014, *A&A*, 566, A34  
 Kral Q. et al., 2017, *Astron. Rev.*, 13, 69  
 Kral Q., Thébaud P., Augereau J.-C., Boccaletti A., Charnoz S., 2015, *A&A*, 573, A39  
 Kral Q., Wyatt M., Carswell R. F., Pringle J. E., Matrà L., Juhász A., 2016, *MNRAS*, 461, 845  
 Lebreton J., Beichman C., Bryden G., Defrère D., Mennesson B., Millan-Gabet R., Boccaletti A., 2016, *ApJ*, 817, 165  
 Levison H. F., Duncan M. J., 1997, *Icarus*, 127, 13  
 Levison H. F., Duncan M. J., Wetherill G. W., 1994, *Nature*, 372, 441  
 Levison H. F., Duncan M. J., Zahnle K., Holman M., Dones L., 2000, *Icarus*, 143, 415

- Lissauer J. J., 2007, *ApJ*, 660, L149
- Lisse C. M. et al., 2012, *ApJ*, 747, 93
- Marboeuf U., Bonsor A., Augereau J.-C., 2016, *Planet. Space Sci.*, 133, 47
- Marino S. et al., 2016, *MNRAS*, 460, 2933
- Marino S. et al., 2017a, *MNRAS*, 465, 2595
- Marino S., Wyatt M. C., Kennedy G. M., Holland W., Matrà L., Shannon A., Ivison R. J., 2017b, *MNRAS*, 469, 3518
- Matrà L. et al., 2017a, *MNRAS*, 464, 1415
- Matrà L. et al., 2017b, *ApJ*, 842, 9
- Matthews B. C., Krivov A. V., Wyatt M. C., Bryden G., Eiroa C., 2014, in Beuther H., Klessen R. S., Dullemond C. P., Hennings T., eds, *Protostars and Planets VI*, University of Arizona Press, Tucson. p. 521
- Melis C., Jura M., Albert L., Klein B., Zuckerman B., 2010, *ApJ*, 722, 1078
- Mennesson B. et al., 2014, *ApJ*, 797, 119
- Millholland S., Wang S., Laughlin G., 2017, *ApJ*, 849, L33
- Montesinos B. et al., 2016, *A&A*, 593, A51
- Morbidelli A., 2005, *ArXiv Astrophysics e-prints*
- Morbidelli A., Chambers J., Lunine J. I., Petit J. M., Robert F., Valsecchi G. B., Cyr K. E., 2000, *Meteorit. Planet. Sci.*, 35, 1309
- Mumma M. J., Charnley S. B., 2011, *ARA&A*, 49, 471
- Muñoz-Gutiérrez M. A., Pichardo B., Reyes-Ruiz M., Peimbert A., 2015, *ApJ*, 811, L21
- Murray C. D., Dermott S. F., 1999, *Solar System Dynamics* Cambridge University Press, Cambridge
- Nesvorný D., Roig F., 2001, *Icarus*, 150, 104
- Nesvorný D., Jenniskens P., Levison H. F., Bottke W. F., Vokrouhlický D., Gounelle M., 2010, *ApJ*, 713, 816
- Nuñez P. D. et al., 2017, *A&A*, 608, A113
- O'Brien D. P., Morbidelli A., Levison H. F., 2006, *Icarus*, 184, 39
- Pu B., Wu Y., 2015, *ApJ*, 807, 44
- Raymond S. N., Izidoro A., 2017, *Icarus*, 297, 134
- Raymond S. N., Scalzo J., Meadows V. S., 2007, *ApJ*, 669, 606
- Raymond S. N., O'Brien D. P., Morbidelli A., Kaib N. A., 2009, *Icarus*, 203, 644
- Rieke G. H., Gáspár A., Ballering N. P., 2016, *ApJ*, 816, 50
- Schüppler C., Krivov A. V., Löhne T., Booth M., Kirchschrager F., Wolf S., 2016, *MNRAS*, 461, 2146
- Smith A. W., Lissauer J. J., 2009, *Icarus*, 201, 381
- Smith R., Wyatt M. C., Haniff C. A., 2009, *A&A*, 503, 265
- Stencel R. E., Backman D. E., 1991, *ApJS*, 75, 905
- Su K. Y. L. et al., 2006, *ApJ*, 653, 675
- Su K. Y. L. et al., 2013, *ApJ*, 763, 118
- Thureau N. D. et al., 2014, *MNRAS*, 445, 2558
- Tisserand F., 1896, *Traité de mécanique céleste*. No. v. 4 in *Traité de mécanique céleste*. Gauthier-Villars, Paris, (Available at: <https://books.google.co.uk/books?id=hNjinQAACAAJ>)
- Trigo-Rodríguez J. M., Saladino R., Di Mauro E., Rotelli L., Moyano-Camero C. E., Carota E., Botta L., 2017, in 48th Lunar and Planetary Science Conference, held 20-24 March 2017, at The Woodlands, Texas, LPI Contribution No. 1964
- van Lieshout R., Dominik C., Kama M., Min M., 2014, *A&A*, 571, A51
- Veras D., Evans N. W., 2013, *MNRAS*, 430, 403
- Veras D., Mustill A. J., Bonsor A., Wyatt M. C., 2013, *MNRAS*, 431, 1686
- Weiss L. M. et al., 2018, *AJ*, 155, 48
- Weissman P. R., 1980, *A&A*, 85, 191
- Wisdom J., 1980, *AJ*, 85, 1122
- Wyatt M. C., Greaves J. S., Dent W. R. F., Coulson I. M., 2005, *ApJ*, 620, 492
- Wyatt M. C., Smith R., Greaves J. S., Beichman C. A., Bryden G., Lisse C. M., 2007a, *ApJ*, 658, 569
- Wyatt M. C., Smith R., Su K. Y. L., Rieke G. H., Greaves J. S., Beichman C. A., Bryden G., 2007b, *ApJ*, 663, 365
- Wyatt M. C., Farihi J., Pringle J. E., Bonsor A., 2014, *MNRAS*, 439, 3371
- Wyatt M. C., Bonsor A., Jackson A. P., Marino S., Shannon A., 2017, *MNRAS*, 464, 3385
- Zuckerman B., Koester D., Reid I. N., Hünsch M., 2003, *ApJ*, 596, 477
- Zuckerman B., Melis C., Klein B., Koester D., Jura M., 2010, *ApJ*, 722, 725

## APPENDIX A: VARYING THE INITIAL $e$ AND $I$

In order to test the effect of our initial conditions on  $e$  and  $I$ , i.e.  $e_{\max} = 0.02$  and  $I_{\max} = 10^\circ$ , we repeat our simulations twice for the reference planet configuration, but changing (i)  $e_{\max}$  to 0.2 and (ii)  $I_{\max}$  to  $1.1^\circ$ . In the first case, the minimum Tisserand parameter and pericentre are reduced from 2.97 to 2.93 and from 18 to 13 au, respectively. The fraction of particles ejected stays roughly the same around 93 per cent, the time-scale for ejection decreases from 120 to 95 Myr, the number of trojans decreases from 30 to 22 per cent,  $f_{\text{in}}$  increases marginally from  $3.7 \pm 0.8$  to  $4.8 \pm 0.8$  per cent, and  $f_{\text{acc, p}}$  decreases from  $0.35 \pm 0.17$  to  $0.25 \pm 0.13$  per cent, although the changes in  $f_{\text{in}}$  and  $f_{\text{acc, p}}$  are still consistent within errors. On the other hand,  $\Sigma(r)$  stays roughly constant.

In the second case, the minimum Tisserand parameter increases to 2.999 and the minimum pericentre to 27 au, near the orbit of the second outermost planet. The fraction of particles ejected decreases slightly to 91 per cent, the ejection time-scale increases to 124 Myr, the fraction of trojans stays the same,  $f_{\text{in}}$  increases marginally to  $4.1 \pm 0.9$  per cent, and  $f_{\text{acc, p}}$  decreases to  $0.15^{+0.16}_{-0.08}$  per cent, although both consistent within errors with our reference system. We also find that  $\Sigma(r)$  stays roughly constant.

These results show that reducing the initial inclination of particles has no significant effect on our results. Increasing the initial eccentricities, however, could increase slightly the amount of material that gets to 0.5 au and decrease the amount of material that is accreted by inner planets. Note that an eccentricity of 0.2 is at the limit of what we would expect in a cold exo-Kuiper belt that has not been perturbed by an eccentric planet (e.g. Kenyon & Bromley 2008). Therefore, we expect that the results and trends found in this paper are robust against different initial eccentricities or inclinations.

## APPENDIX B: VARYING THE LENGTH OF SIMULATIONS

To test if our results are dependent on the length of our simulations, we extended the integration to 5 Gyr for the planet configuration that had the slowest evolution. This is the system of 10  $M_{\oplus}$  planets spaced with  $K = 20$ . We find that the time-scale for ejection was correctly estimated being  $570 \pm 35$  Myr, even though a significant fraction of the particles had not been ejected after 1 Gyr. The fraction of ejected particles increased slightly from 90 to 92 per cent, but consistent within errors. We also find that  $f_{\text{in}}$  and the fraction of accreted particles per inner planet are slightly lower, but consistent with our previous estimate given uncertainties. Finally, we find that the derived steady-state surface density is consistent with one derived only considering 1 Gyr of evolution. We conclude that 1 Gyr is enough time to understand the behaviour of these systems with outer planets with masses  $\gtrsim 10 M_{\oplus}$  and our results and conclusions would not change significantly by extending the length of our simulations.

## APPENDIX C: VARYING THE INNER BOUNDARY TO 0.1 AU

In our simulations we remove particles with a pericentre lower than 0.5 au for two reasons, to keep track of how many particles get to the very inner regions, and because we cannot rely on orbits within 0.5 au as we use a time-step of 30 d. To explore the effects that this causes, for example in the surface density and the number of impacts on inner planets, we moved our inner edge to 0.1 au, reducing the time-step of the integration to 3 d, but without adding extra

planets. As expected, the number of particles that cross the inner edge decreased from 3.7 to 1.5 per cent. The fraction of particles ejected increased slightly and the fraction accreted stayed roughly constant. We also find that the surface density only changes within 4 au, where it is higher compared to our reference system as particles that were previously removed stay in the system for longer. The fraction of particles accreted per inner planet did not increase significantly because only one of the three inner planets resides

within 4 au, where  $\Sigma(r)$  increased. Moreover, the new particles able to remain with the lower inner edge are highly eccentric, hence less likely to be accreted. Based on this surface density, we derive a power-law index of 0.3 between 1 and 50 au, flatter than derived before.

This paper has been typeset from a  $\text{\TeX/L\AA\TeX}$  file prepared by the author.